
ManiBox: Enhancing Embodied Spatial Generalization via Scalable Simulation Data Generations

Hengkai Tan^{1*}, Xuezhou Xu^{2*}, Chengyang Ying^{1*}, Xinyi Mao¹, Zeyuan Wang¹,
 Songming Liu¹, Xingxing Zhang¹, Zhizhong Su³, Hang Su¹, Jun Zhu¹

¹Tsinghua University ²National University of Singapore ³Horizon Robotics
 thj23@mails.tsinghua.edu.cn, xu.xuezhou@u.nus.edu, ycy21@mails.tsinghua.edu.cn

Abstract

Embodied agents require robust spatial intelligence to execute precise real-world manipulations. However, this remains a significant challenge, as current methods often struggle to accurately position objects in space. Collecting extensive data can help address this issue by enhancing the agent’s spatial understanding. Nonetheless, obtaining such data with real robots is prohibitively expensive, and relying on simulation data frequently leads to visual generalization gaps during real-world deployment. To tackle these challenges, we propose **ManiBox**, a novel bounding-box-guided framework. By decoupling perception from policy generalization, ManiBox effectively reduces the Sim2Real gap, leverages Internet-scale data, and scales our policy data collection in simulation. Specifically, within ManiBox, the RL teacher policy efficiently generates scalable simulation data. The student policy is distilled from this data and takes bounding boxes as input, which is proven sufficient for determining objects’ spatial positions, thus enabling zero-shot transfer to real robots. Comprehensive evaluations in both simulated and real-world environments demonstrate that ManiBox exhibits strong spatial generalization and adaptability across various manipulation tasks and settings. Furthermore, our empirical study provides preliminary verification of spatial scaling laws, i.e., the amount of data required for spatial generalization scales with spatial volume following a power-law relationship. At a given spatial volume level, the success rate of manipulation tasks follows Michaelis-Menten kinetics with respect to data volume, exhibiting a saturation effect as data increases.²

1 Introduction

Spatially accurate robotic manipulation in dynamic environments is crucial for advancing modern robotics [10]. Enabling precise manipulation in unstructured settings extends robots’ utility beyond static environments and enhances their real-world effectiveness, particularly in industrial and domestic applications. A key requirement for such systems is the development of **spatial generalization**—*the ability of a manipulation agent to complete tasks regardless of the target object’s position within a defined spatial volume*. This generalization is crucial for varying real-world spatial conditions, where the objects are rarely fixed in place.

Recent work has made notable progress in embodied manipulation in different tasks or environments, such as large embodied foundation models driven by end-to-end training [1, 37, 2, 38, 53, 19].

*Equal contribution

²Our videos and code are available in the [project page](#)

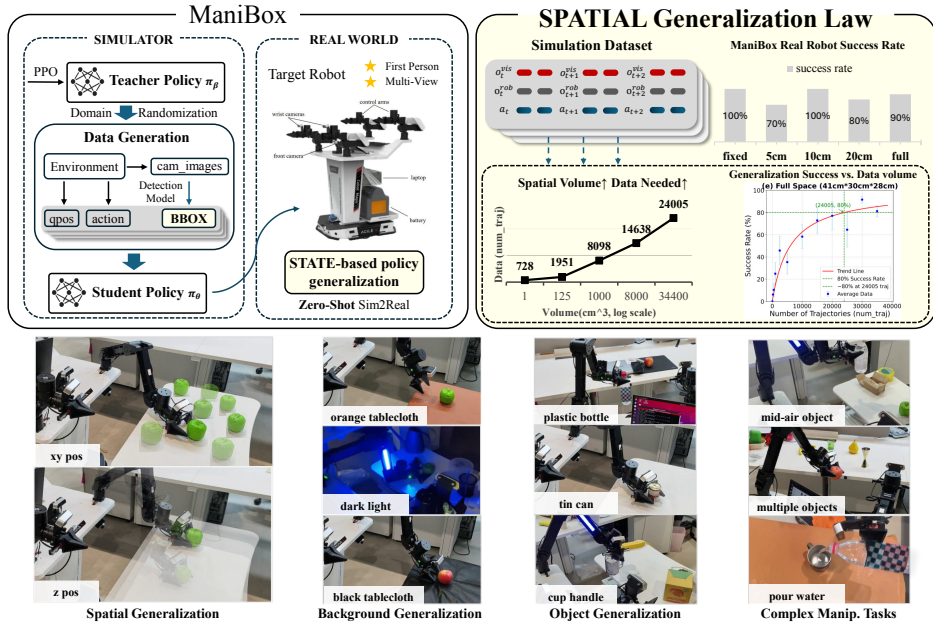


Figure 1: Overview. We introduce ManiBox, a bbox-guided manipulation method using a teacher-student framework to enhance embodied spatial generalization. We reveal that spatial volume generalization scales positively with data volume in a power law, with manipulation success following Michaelis-Menten kinetics relative to data volume for specified spatial volumes. Extensive real-world tests show ManiBox’s robust adaptability to varied spatial positions, objects, and backgrounds.

However, these models still lack sufficient spatial awareness and reasoning capabilities, posing substantial challenges for spatial generalization in real-world applications [6]. Our analysis (Lemma 3.1) suggests that achieving spatial generalization over larger volumes requires substantially more data, a relationship we also empirically verify as a power law (Figure 3b). For example, training a grasping policy at a fixed point may only require 50 to 600 trajectories. However, when the grasping policy need to generalize within a spatial volume of $34,400\text{cm}^3$ ($41\text{cm} \times 30\text{cm} \times 28\text{cm}$, roughly the maximum reach of our robotic arm), the required data increases $34400^{0.35} = 38$ times, demanding tens of thousands of trajectories.

Unfortunately, existing robotic action trajectories for embodied foundation models is significantly more scarce on the internet compared to image datasets. And collecting such large data on real robots to achieve spatial generalization is prohibitively expensive. For example, RT-1 spends 17 months accumulating 130K episodes [2], a level of resource commitment that is unfeasible for most researchers. Although simulation data can help bridge this gap, significant high-dimensional visual discrepancies between simulated and real environments, known as the Sim2Real gap, also pose additional challenges. While prior efforts have aimed to enhance performance using various visual generalization techniques, each method has limitations. Some require unobstructed third-person perspectives [50], while others demand substantial computational resources [38, 1]. These constraints hinder real-time processing and practical deployment on resource-limited robotic platforms.

To bridge this gap, we propose decoupling observation perception from policy generalization, which helps reduce the Sim2Real gap and enhance spatial generalization. First, instead of training image-based policies, we choose visual intermediate representations like bounding-box as the policy inputs. This choice can utilize internet-scale datasets to improve visual representation learning and significantly reduce the Sim2Real gap compared with the original images. Although visual intermediate representations may lose some information, our lemma 3.2 demonstrates the completeness of bounding boxes captured from multiple cameras; that is, they can effectively encapsulate the 3D structure of convex objects. Moreover, taking visual intermediate representations as the input is beneficial for **scaling up the collected action data in simulators** and improving the policy generalization by reducing the Sim2Real gap, which can also facilitate spatial generalization, even when the visual representations are biased. Based on these observations, we propose a novel bounding-box-guided methodology **ManiBox** (Figure 1) to enhance spatial generalization and adaptability. In detail, ManiBox first trains a teacher policy with privileged information in the simulator with reinforcement

learning (RL). This policy then generates scalable robot trajectories, replacing traditional visual inputs with bounding box coordinates to facilitate spatial generalization of manipulation policies. Subsequently, the student policy trained on these simulation data achieves robust zero-shot transfer to real-world tasks, leveraging bounding boxes identified by advanced open-vocabulary detection models, such as YOLO-World [7].

Extensive experiments in both simulators and real robots demonstrate a direct correlation between data volume and spatial generalization performance: *more data consistently leads to higher success rates, and generalizing to larger spatial volumes requires even more data*. The success rate and the data volume show the **Michaelis-Menten kinetic curve**. And the data volume required for spatial generalization is related to the spatial volume in a **power-law relationship**. For example, to reliably grasp objects within a 34400cm^3 workspace, tens of thousands of trajectories from various positions are required. ManiBox achieves nearly perfect success rates in real-world grasping tasks by leveraging large-scale simulation data generated across diverse spatial volumes. Furthermore, ManiBox is flexible for handling different manipulation tasks and exhibits robust generalization in new scenarios, including unfamiliar object types, complex surfaces, changing lighting conditions, and environments with distractions.

Our contributions include: (1) We propose **ManiBox**, a novel framework that decouples visual representation from policy generalization to reduce the Sim2Real gap and scale up simulation data; (2) ManiBox significantly enhances adaptability across diverse spatial positions, object types, and backgrounds, as demonstrated by extensive evaluations in both simulated and real-world environments. (3) We take an initial step in unveiling the impact of data volume on spatial generalization through scalable data generation, laying the foundation for improving generalization in embodied systems.

2 Related Work

Generalization for Robotic Manipulation. Generalization is fundamental and significant for robotic manipulation, especially in dynamic environments with varying visual inputs and changing conditions. Existing vision-based policy generalization methods leverage both simulated and real-world data. By simulating diverse visual scenarios, robots can better generalize to new environments and tasks. For instance, multi-task and multi-object manipulation studies have extended behavior cloning to handle different visual inputs, improving generalization to unseen objects and scenes [44, 9]. Additionally, language-conditioned policies [2, 53, 38] and imitation learning from human videos [4, 31] enable robots to manipulate objects using both visual and language cues. While methods like bounding box annotations assist in specific tasks, such as pose estimation [16], understanding the relationship between dataset scale and generalization remains an area that requires further exploration.

Embodied Learning from Simulation. Simulators provide an efficient and scalable way to expand embodiment datasets, offering a cost-effective means for parallel data collection and faster iteration cycles. There are three main approaches: 1) training RL agents through interaction within the simulator [16, 34, 50], 2) mimicking expert demonstrations generated in simulation with imitation learning [47, 41, 29], and 3) employing teacher-student frameworks, i.e., training a teacher policy with privileged information to guide a student policy [21, 11, 52]. One of the major challenges of utilizing simulation data is the Sim2Real gap. Various techniques have been developed to bridge it, including realistic simulators [43, 17, 26], domain randomization [42, 33, 52], and vision-based policy generalization [11, 41, 49, 50]. These approaches enable robots to generalize across diverse visual and physical conditions, which are critical in real-world environments. While real-world datasets such as Open X-Embodiment [32] provide 1M demonstrations, they are much smaller than datasets in other domains like language and images [23, 30, 45, 46]. Thus, simulation-generated datasets play a vital role in compensating for the limitations of real-world data collection.

3 Methodology

In this section, we first formulate the problem and then introduce our ManiBox, including teacher policy training, simulation data generation, and student policy distillation.

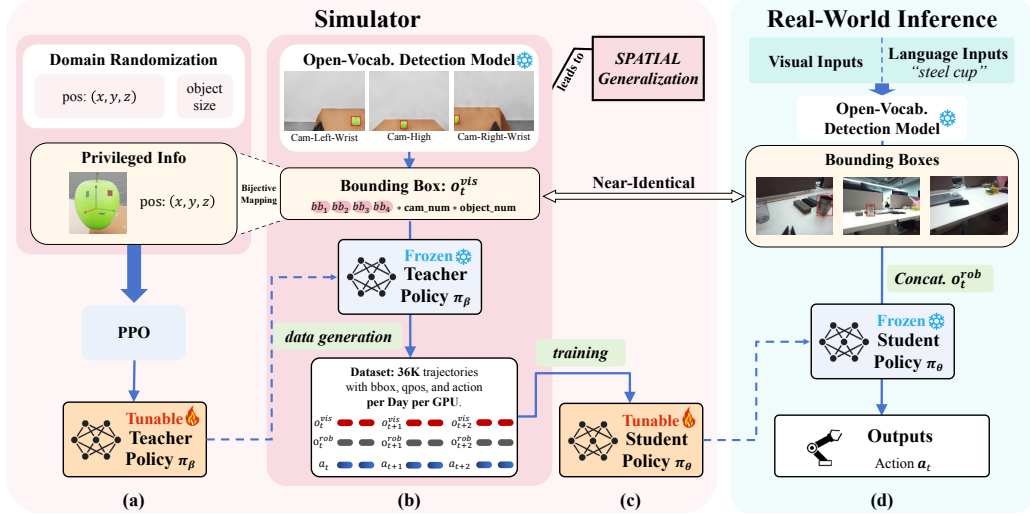


Figure 2: **ManiBox illustration.** (a) Utilizing PPO and domain randomization, we train a sophisticated teacher policy in the simulator that utilizes privileged object information to determine actions. (b) The teacher policy generates scalable trajectory data, utilizing bounding box coordinates instead of traditional high-dimensional visual inputs or privileged information. (c) A state-based student policy, generalizable and capable of zero-shot transfer, is trained on this extensive simulation dataset, greatly improving spatial generalization. (d) Guided by bounding boxes, the student policy precisely executes actions for real robots, achieving improved generalization capabilities.

3.1 Problem Formulation

For robotic manipulation within dynamic environments, achieving spatial generalization (i.e., the ability to effectively perform tasks across varied spatial configurations) is essential for usability and overall efficacy. We formulate it as a partially observable Markov decision process (POMDP) [3] as the robot cannot access to complete state information, especially in real-world settings. Formally, we consider the POMDP $\mathcal{M} = (\mathcal{S}, \mathcal{A}, \mathcal{O}, \mathcal{T}, \mathcal{R}, \gamma)$, where \mathcal{S} represents the state space, including all configurations of the robot and its environment; \mathcal{A} denotes the action space, containing all possible robot actions; \mathcal{O} is the observation space, which reflects the limited state information accessible to the robot; $\mathcal{T}(s_{t+1}|s_t, a_t)$ and $\mathcal{R}(s_t, a_t)$ are the state transition dynamics; and the reward function, respectively; and γ is the discount factor.

In real-world scenarios, the robot receives partial observations $\mathcal{O}_t \in \mathcal{O}$, which provides incomplete and potentially noisy information about the true state s_t . The robot's objective is to find a policy π that maps observations (or histories of observations) to actions $a_t \sim \pi(a_t|\tau_t)$, where $\tau_t = (\mathcal{O}_0, a_0, \mathcal{O}_1, \dots, \mathcal{O}_t)$ is the history. The policy requires maximizing the expected cumulative reward:

$$J(\pi) = \mathbb{E}_{\tau \sim \pi} \left[\sum_{t=0}^{\infty} \gamma^t \mathcal{R}(s_t, a_t) \right]. \quad (1)$$

However, solving POMDPs for manipulation tasks is computationally expensive, as it requires the belief distribution over all possible states, including the precise position, orientation, and object dynamics. This complexity is compounded by the need to handle occlusions, sensor noise, and dynamic changes in the environment, making it challenging for robots to operate efficiently in real-world settings where the state is constantly evolving and uncertain [18, 20].

To reduce this complexity and improve the real-world spatial generalization, we develop **ManiBox**, a novel bounding-box-guided manipulation method by adopting the teacher-student framework [21, 11]. First, ManiBox enables efficient, scalable data generation, as the teacher policy in simulation can produce a large and diverse set of trajectories. Moreover, with low-dimensional bounding box states, ManiBox effectively reduces the Sim2Real gap and accelerates the training of the student policy.

However, due to the complexity of real-world manipulation, there are several notable challenges in designing ManiBox. First, the teacher policy must efficiently explore high-dimensional state spaces in simulation, which are computationally intensive. The student policy needs to handle incomplete

observations and adjust to real-world variations, such as sensor noise and dynamic environmental conditions not present in simulations. Below, we will introduce core concepts of Manibox for overcoming these challenges and show that Manibox is flexible to handle different manipulation tasks in our experiments. The pseudo algorithm of ManiBox can be seen in Alg. 1.

3.2 Teacher Policy Training

To automatically and efficiently generate a large amount of diverse data, we first train an expert **teacher policy** $\pi_\beta : \mathcal{S} \rightarrow \mathcal{A}$ in the simulation where it can access the full state information s_t , including privileged information such as precise object positions. We optimize π_β with Proximal Policy Optimization (PPO) [35] by maximizing the expected reward $J(\pi_\beta)$, where the reward function is designed to handle the manipulation task. Especially, there are several advantages of the choice of lower-dimensional states in teacher policy: benefiting efficient learning, reducing exploration space through privileged information, and supporting larger parallel environments. To leverage these benefits, we carefully design the simulation environment to reduce the exploration space and make it easier for the policy π_β to find the point with the highest return below (More details are in Appendix F.1):

Environment Setup. To ensure efficient policy training and data generation, we utilize Isaac Lab [28], which supports large-scale parallelism environments. The scene includes a platform, a robot, and objects arranged simply to facilitate future domain randomization. We apply the dual-arm Mobile ALOHA [10] robot, equipped with three first-person-view RGB cameras, into the simulator and ensure its dynamics are consistent with the real world.

State. As mentioned above, our teacher policy take the full state information s_t as the input, including privileged information, which can accelerate RL training and benefit learning generalized policies.

Domain Randomization. To improve the generalization of the teacher policy and enhance the spatial diversity of the generated data, we adopt several domain randomization techniques:

- *objective position* (x, y, z) : To improve the spatial generalization of the teacher policy to the whole space, we apply the domain randomization for all three dimensions of x , y , and z , ensuring that the x -coordinate and y -coordinate of the object can cover a large range. Moreover, the height of the platform is randomized to ensure that the z -coordinate of the object in the data can cover the feasible working space of the robotic arm.
- *object size*: To ensure that the agent can manipulate objects of *various sizes*, we also randomize the size of the object.

These two domain randomization techniques allow the teacher policy to manipulate different objects of different positions and sizes, which is significant for real-world spatial and object generalization.

3.3 Simulation Data Generation

After training the teacher policy, it can automatically generate data for training the student policy that can be deployed in the real world across different objects, spatial positions, and backgrounds.

Data Volume Estimation. To guide the data volume needed for policy generalization to a specific spatial volume, we analyze the sample efficiency for generalizing in a $b \times b \times b$ cube. Based on the classical learning theory, the sample complexity of the uniform convergence property is in proportion to the VC dimension of the model hypothesis set [36]. Extending previous results about generalization bounds for multi-task learning [8], we can prove:

Lemma 3.1 (Details are in Appendix A.1). *For training a manipulating agent that can generalize spatially within a cube whose size is $b \times b \times b$ via imitation learning, under some mild assumptions in [8], the VC dimension is at most proportional to $d \log(Cb^3d)$, where d is the VC dimension of the hypothesis set for manipulating the fixed point and C is a constant independent of d, b .*

Lemma 3.1 demonstrates that the data required for policy generalization to a certain volume grows. Consequently, training a student policy feasible under full spatial range requires a large scale of trajectories, which needs efficient data generation and collection.

On the other hand, as we cannot access the privileged information in the real world, the student policy needs visual observations that implicitly encode object position information. However, the Sim2Real gap between visual images in the simulator and the real world is significant due to the vast complexity of real-world environments (e.g., various backgrounds and objects). To address this Sim2Real gap

and enable robust spatial generalization, we propose using an individual vision module to extract the bounding box from camera views as a **consistent, low-dimensional, and complete** representation of the object’s spatial properties, such as position and size.

Bounding Boxes Provides Sufficient 3D Information of Objects. To efficiently generate a large amount of simulator data that aligns with real-world visual images, the vision module must be robust and efficient. Considering open-vocabulary detection, we selected YOLO-World [7] as the frozen 2D visual feature extraction module. This provides us with the bounding box of the objects as a 2D low-dimensional visual feature, which is consistent and low-dimensional. Notably, the inference time of YOLO-World for a single image is around 30ms, ensuring the efficiency of real-world inference.

Moreover, although 2D low-dimensional visual features may lose several information in images, we demonstrate that they are sufficient for manipulation as they can contain the full complete information about object position and size by presenting the following lemma, i.e., the 3D information of a sphere can be uniquely determined by the bounding boxes from two cameras:

Lemma 3.2 (Details and proofs are in Appendix A.2). *Given: (1) Two pinhole cameras with known intrinsic parameters K_i and extrinsic parameters (R_i, t_i) ; (2) A sphere of unknown radius r is fully visible in both camera images without occlusion; (3) Normalized image coordinates of the bounding boxes of the sphere in both images: Camera i : $(u_{1\min}, v_{1\min}, u_{1\max}, v_{1\max})$, the image dimensions are known (width W_i and height H_i for each camera).*

Then the 3D coordinates of the sphere’s center C and radius r in the world coordinate system can be uniquely determined with the known camera parameters and the normalized bounding box coordinates, provided that the cameras are not in degenerate configurations.

Lemma 3.2 illustrates that the 3D position information of a sphere can be implied by utilizing multi-view bounding boxes [13], indicating that Manibox can capture complete spatial position information of target objects for real-world control policies.

In short, by using an individual vision module, Manibox mitigates the Sim2Real gap by providing the student policy with consistent input across both the simulation and the real world. Specifically, the student policy receives both proprioceptive data o_t^{rob} and bounding box data o_t^{vis} as inputs:

$$\pi_\theta : \mathcal{O} = \mathcal{O}_{\text{rob}} \times \mathcal{O}_{\text{vis}} \rightarrow \mathcal{A}. \quad (2)$$

3.4 Student Policy Distillation

After collecting expert data from the teacher policy in the simulator, we distill the student policy with this expert data. Then, we can directly deploy the student policy on the robot in the real world, which poses extra challenges compared with the simulation, such as sensor noise and dynamic environments.

For example, open-vocabulary detection models may fail to recognize real-world target objects at times because of background distraction or robot gripper occlusion, while the recognition of the simulated target object rarely fails. To address this challenge, we introduce the random mask. In detail, when distilling the student policy with the simulation expert data \mathcal{D} , we randomly mask some bboxes (i.e., set to 0) with a predefined probability of `random_mask_ratio`, indicating that this camera may not recognize the target object and imitating the real-world scenarios in which the open-vocabulary detection model fails to generate the bounding box.

Moreover, based on the real-world partial observability, our student policy requires encoding sufficient history information [12, 22, 48] and thus utilizes RNN as:

$$\mathbf{x}_t, \mathbf{h}_t = \text{LSTM}(\mathbf{s}'_t, \mathbf{h}_{t-1}), \quad \mathbf{a}_t = \text{FC}_2(\text{drop}(\text{gelu}(\text{FC}_1(\mathbf{x}_t))). \quad (3)$$

where \mathbf{s}'_t and \mathbf{h}_t denote the input state and the hidden state of the LSTM at time t , \mathbf{x}_t is the intermediate output of the LSTM, and \mathbf{a}_t is the action vector output by the policy. Furthermore, $\text{LSTM}(\cdot)$, $\text{gelu}(\cdot)$, $\text{drop}(\cdot)$, $\text{FC}(\cdot)$ represent the Long Short-Term Memory (LSTM) [15], Gaussian Error Linear Unit (GELU) activation [14], dropout [40], and Fully Connected (FC) layer, respectively.

The combination of random mask and trajectory modeling significantly contributes to robustness and generalization in deploying our student policy, conquering the challenge of partial observations and unseen real-world variations. (More Sim2Real techniques are in Appendix F.4)

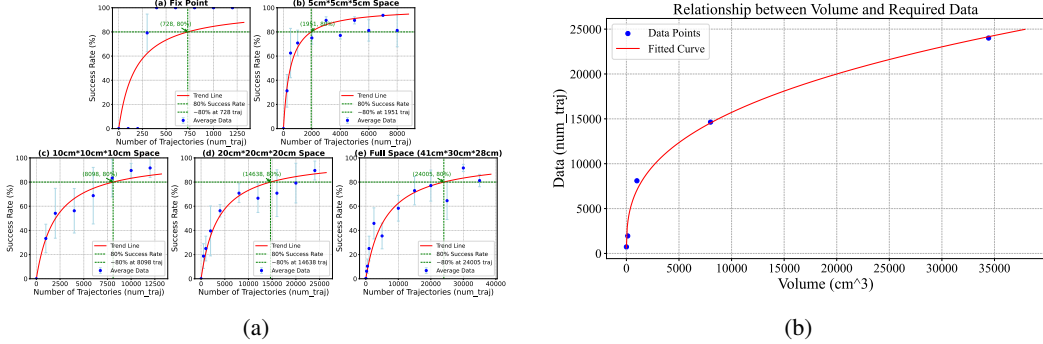


Figure 3: (a) **The scaling relationship between spatial generalization and data volume in grasping**, under different spatial ranges. Data volume represents the number of trajectories used to train the student policy. The estimated 80% success point is marked, with blue points showing the average success rate across 3 seeds and error bars indicating standard deviation. The curve corresponding to the other tasks is detailed in Appendix D. (b) The relationship between spatial volume and data needed to reach 80% grasping success rate. The fitted curve represents a power function $y = 640.32 \cdot x^{0.35}$.

Method	Inverse Kinematics	Key Steps	w/r Random Mask	ManiBox (Ours)
SR of Full Space	$68.75\% \pm 5.10\%$	$6.25\% \pm 8.84\%$	$58.33\% \pm 7.80\%$	$91.67\% \pm 2.95\%$

Table 1: The simulator success rate (SR) on the full space.

4 Experiments

In this section, we conduct extensive experiments in both the simulator and real world, covering various backgrounds, objects, and positions to answer the following questions: (1) What is the scaling relationship between spatial generalization and data amounts in manipulation? (Sec. 4.2) and (2) What about the efficacy of Manibox in real-world applications, especially the generalization ability to different backgrounds, objects, and object spatial positions? (Sec. 4.3)

4.1 Experimental Setup

Real Robot. Mobile ALOHA [10] is a cost-effective and highly stable robot designed for manipulation tasks. Each subordinate arm of Mobile ALOHA is fitted with an RGB camera on its wrist, complemented by another RGB camera centrally mounted on the robot’s body. These three RGB images are taken as observations. Mobile ALOHA has demonstrated strong generalization capabilities across a diverse range of complex manipulation tasks, making it an ideal choice for deploying Manibox.

Tasks. We choose several manipulation tasks to validate the generalization of Manibox. For each task, such as grasping an apple or pouring water from a bottle into a cup, we randomly place the object on a table on a spatial volume $41cm * 30cm * 28cm$ (length * width * height), which is roughly the maximum reach of our robotic arm and referred as “**Full Space**”. Also, to demonstrate the generalizability, real-world counterparts are established with alternative objects and backgrounds.

4.2 Spatial Scaling Law with Data

To guide us in determining the data volume required for a certain level of spatial generalization, we investigate the relationship between policy performance and data volume. We conduct extensive experiments in the simulator to evaluate the success rate (**SR**) of policies trained on different data volumes. We select five distinct spatial ranges to explore this scaling behavior, including the fixed range and four dynamic ranges of 5, 10, 20 units, and full space. For each spatial range, we select more than 8 data volumes to train the student policy and evaluate its grasping SR at random positions.

Fig. 3a shows the **Michaelis-Menten kinetic curve** between the SR and the volume of the data: when the data volume is zero for each spatial range, the policy inevitably fails; as the data volume increases, the manipulation policy’s SR improves, but the growth slows down. Eventually, the SR tends to be **saturated** because of the regret problem and is infinitely close to 100%. The relationship

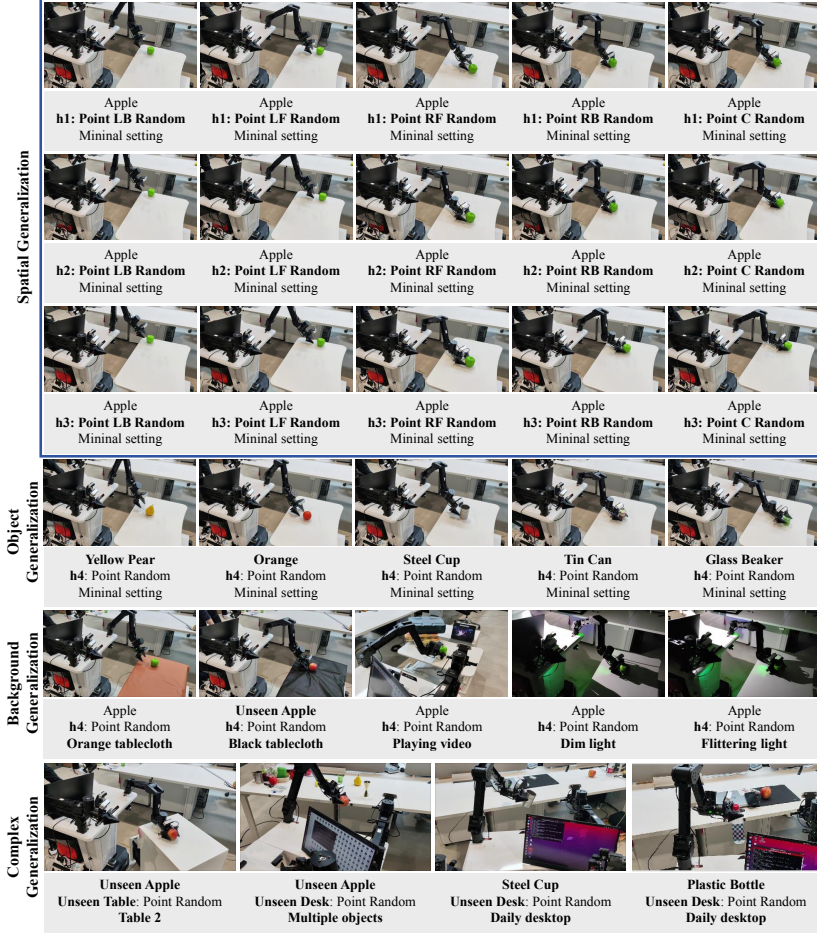


Figure 4: Demonstration of the generalization of Manibox across different backgrounds, objects, and positions. The h1, h2, h3, and h4 are approximately 57cm, 65cm, 72cm, and 65cm, which are randomly selected object heights based on the height of our robot. LB, LF, RF, RB, and C are abbreviations for Left-Back, Left-Front, Right-Front, Right-Back, and Center area, respectively.

between the SR and the data volume is **expressed by the formula**: $SR = \frac{100\% * D}{K_m + D}$, where D is the data volume of the imitation policy, K_m is the data volume required to achieve 50% SR.

Furthermore, we identify the data volume required to achieve an 80% SR for each spatial range (Fig. 3a) and find that the spatial volume and the required data follow a **power law relationship** (Fig. 3b). In other words, the data volume required for spatial generalization is related to the spatial volume in a power-law relationship, i.e., more data improves the ability to generalize over a larger spatial range. For example, to achieve spatial generalization across an x -fold increase in volume, the required data volume scales approximately as $x^{0.35}$. In our experimental setup, generalizing from 1cm^3 to 34400cm^3 necessitates a $34400^{0.35} \approx 38$ -fold increase in data volume. Such large-scale data collection would be expensive in the real world, emphasizing the significance of simulation data, which is more affordable and efficient. To further demonstrate the importance of other variables (e.g., time) in spatial intelligence and the robustness of policy generalization to visual uncertainty, we have provided detailed ablation experiments on the spatial intelligence of Manibox in Appendix B.

4.3 Real-world Results

To validate the generalization ability of Manibox in the real world, we deploy student policies trained on simulation data into a real robot and test the performance across multiple arbitrarily chosen positions, eight objects (some are out-of-distribution), five backgrounds, and three complex settings, as illustrated in Figure 4. More details of these experiments are in the Appendix E.3.

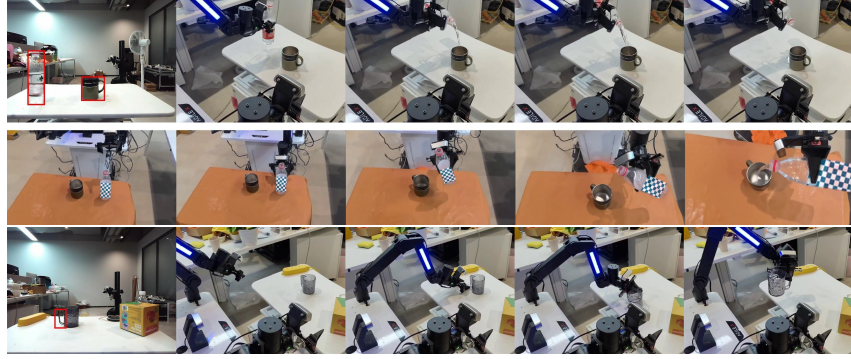


Figure 5: **Pour Water (the above two rows):** The robot grasps the left water bottle and pours water into the right cup, demonstrating the extensibility of Manibox to more complex tasks. **Grab the handle of the cup (the last row):** Manibox is flexible to combine with more fine-grained visual models like [24] to achieve more complicated manipulation tasks. We take grabbing the handle of a cup as an example. The first figure shows the recognition of the cup handle from the first-person view, and other figures show the task completion process from the third-person view.

Spatial generalization. To evaluate the generalization capability of Manibox, we evaluate the student policy across four spatial volumes and a fixed point. For each experiment, we randomly place an apple on the table at arbitrarily chosen heights within the given range (as illustrated in the first three rows of Fig. 4). Alongside the difference in form and appearance, the apple presents considerable unpredictability to the visual detection model due to factors including background, lighting, target object, etc. Consequently, the bounding box varies in size or even disappears at most of the time, emphasizing the need for robustness of the policy. As shown in Tab. 6 (Appendix E.4), Manibox generalizes well to objects falling in different spatial volumes, achieving the SR between 70%-100%. In contrast, vision-based ACT, which trains the student policy with the vision input ACT [51] on video-action simulation data, experiences a visible drop in SR when spatial range scales up due to the Sim2Real gap, despite its considerable SR of 70% on a fixed point. The results demonstrate that Manibox harbors strong generalization when addressing uncertainties arising from real-world objects, variations in spatial positions, and visual detection interferences.

Object generalization. To justify Manibox’s object generalization ability, we chose eight objects: the original apple, unseen apple, yellow pear, orange, steel cup, tin can, glass beaker, and plastic bottle. For each object, the open-vocabulary visual detection model and obtain the bounding box from the corresponding name, which is enough for the policy to grasp the target object. It is worth noting that five of the selected objects are out-of-distribution in size (their bounding box sizes are unseen in the simulation data), which further illustrates the object generalization ability of Manibox. The ability to generalize across objects, even with significantly different bounding boxes, aligns with our Lemma 3.2, which proves that the 3D position information of the object is complete in the dataset.

Background Generalization. The open-vocab perception models (e.g. YOLO-World) and learning from trajectories enable ManiBox to generalize across vision backgrounds without extra visual domain randomization. To verify it, we consider three table shapes, two tablecloths colors, as well as three lighting conditions: a single stationary point light source, a single flickering point light, and playing videos in the background. Furthermore, we construct two more complex scenarios: a multi-object environment and a typical daily workplace desktop. The results demonstrate Manibox’s strong background generalization ability. Even in dark environments, the detection model fails to detect the target object most of the time, **the generalization of Manibox compensates for those visual errors** (Sec. B.2). This can be attributed to Manibox’s endeavor to integrate historical information and random masking to increase the visual model’s tolerance for errors. Details are in Appendix B.

Various manipulation tasks. In Figure 5, we also evaluate more real-world manipulation tasks: **Pour Water** and **Grab the handle of the cup**, showcasing the extensibility of Manibox to multi-object manipulation tasks and the grasping of detailed parts of irregular objects, respectively.

Table 2: Comparison with baselines on RoboTwin tasks (Hard Setting)

Task	ACT	DP	DP3	Ours
Move Can Pot	0%	0%	6%	11%
Grab Roller	25%	0%	2%	43%
Stack Bowls Two	0%	0%	6%	1%
Pick Dual Bottles	0%	0%	1%	1%
Put Bottles Dustbin	1%	0%	21%	1%
Average Success Rate	5.2%	0%	7.2%	11.4%

4.4 Baseline Comparison

We further evaluate ManiBox on multiple manipulation tasks of RoboTwin [5]. Specifically, we select representative tasks spanning bimanual and object-centric scenarios. All policies are trained on the Aloha-AgileX using 50 `demo_clean` demonstrations for each task. All models are evaluated 100 times under `demo_randomized` (Hard) settings, following the official RoboTwin 2.0 protocol. Overall, ManiBox matches or surpasses ACT, DP, and DP3, with clear gains in the challenging Hard settings (Table 2).

5 Conclusion

In this work, we present ManiBox, a novel bounding-box-guided manipulation method to decouple Internet-scale-trained perception models from policy generalization whose action data are scalably collected in the simulator. To reduce the generalization gap in vision-based models from simulator to real-world deployment, ManiBox equips the state-based student policy with bounding-box as visual intermediate inputs. Extensive experiments in both simulated and real-world environments demonstrate that ManiBox significantly outperforms existing methods in adapting across different spatial positions, objects, and background variations. Moreover, our theoretical and empirical analyses reveal that the data volume required for spatial generalization is related to the spatial volume in a power-law relationship, and the SR follows Michaelis-Menten kinetics for specified spatial volumes. These findings pave the way for the development of robust spatial generalization across a wide range of embodied systems. More discussion of the limitations and future work is in Appendix H.

References

- [1] Michael Ahn, Anthony Brohan, Noah Brown, Yevgen Chebotar, Omar Cortes, Byron David, Chelsea Finn, Chuyuan Fu, Keerthana Gopalakrishnan, Karol Hausman, et al. Do as i can, not as i say: Grounding language in robotic affordances. *arXiv preprint arXiv:2204.01691*, 2022.
- [2] Anthony Brohan, Noah Brown, Justice Carbajal, Yevgen Chebotar, Joseph Dabis, Chelsea Finn, Keerthana Gopalakrishnan, Karol Hausman, Alex Herzog, Jasmine Hsu, et al. Rt-1: Robotics transformer for real-world control at scale. *arXiv preprint arXiv:2212.06817*, 2022.
- [3] Anthony R Cassandra, Leslie Pack Kaelbling, and Michael L Littman. Acting optimally in partially observable stochastic domains. In *Aaaai*, volume 94, pages 1023–1028, 1994.
- [4] Annie S Chen, Suraj Nair, and Chelsea Finn. Learning generalizable robotic reward functions from "in-the-wild" human videos. *arXiv preprint arXiv:2103.16817*, 2021.
- [5] Tianxing Chen, Zanxin Chen, Baijun Chen, Zijian Cai, Yibin Liu, Qiwei Liang, Zixuan Li, Xianliang Lin, Yiheng Ge, Zhenyu Gu, et al. Robotwin 2.0: A scalable data generator and benchmark with strong domain randomization for robust bimanual robotic manipulation. *arXiv preprint arXiv:2506.18088*, 2025.
- [6] An-Chieh Cheng, Hongxu Yin, Yang Fu, Qiushan Guo, Ruihan Yang, Jan Kautz, Xiaolong Wang, and Sifei Liu. Spatialrgrpt: Grounded spatial reasoning in vision language model, 2024.
- [7] Tianheng Cheng, Lin Song, Yixiao Ge, Wenyu Liu, Xinggang Wang, and Ying Shan. Yolo-world: Real-time open-vocabulary object detection. In *Proceedings of the IEEE/CVF Conference on Computer Vision and Pattern Recognition*, pages 16901–16911, 2024.
- [8] Koby Crammer and Yishay Mansour. Learning multiple tasks using shared hypotheses. *Advances in Neural Information Processing Systems*, 25, 2012.

[9] Hao-Shu Fang, Chenxi Wang, Hongjie Fang, Minghao Gou, Jirong Liu, Hengxu Yan, Wenhui Liu, Yichen Xie, and Cewu Lu. Anygrasp: Robust and efficient grasp perception in spatial and temporal domains. *IEEE Transactions on Robotics*, 2023.

[10] Zipeng Fu, Tony Z Zhao, and Chelsea Finn. Mobile aloha: Learning bimanual mobile manipulation with low-cost whole-body teleoperation. *arXiv preprint arXiv:2401.02117*, 2024.

[11] Haoran Geng, Ziming Li, Yiran Geng, Jiayi Chen, Hao Dong, and He Wang. Partmanip: Learning cross-category generalizable part manipulation policy from point cloud observations. In *Proceedings of the IEEE/CVF Conference on Computer Vision and Pattern Recognition*, pages 2978–2988, 2023.

[12] Danijar Hafner, Timothy Lillicrap, Jimmy Ba, and Mohammad Norouzi. Dream to control: Learning behaviors by latent imagination. In *International Conference on Learning Representations*, 2020.

[13] Richard Hartley and Andrew Zisserman. *Multiple view geometry in computer vision*. Cambridge university press, 2003.

[14] Dan Hendrycks and Kevin Gimpel. Gaussian error linear units (gelus). *arXiv preprint arXiv:1606.08415*, 2016.

[15] Sepp Hochreiter and Jürgen Schmidhuber. Long short-term memory. *Neural Computation*, 9(8):1735–1780, 1997.

[16] Baichuan Huang, Jingjin Yu, and Siddarth Jain. Earl: Eye-on-hand reinforcement learner for dynamic grasping with active pose estimation. In *2023 IEEE/RSJ International Conference on Intelligent Robots and Systems (IROS)*, pages 2963–2970. IEEE, 2023.

[17] Stephen James, Zicong Ma, David Rovick Arrojo, and Edward Johns. Rlbench: The robot learning benchmark & learning environment. *IEEE Robotics and Automation Letters (RA-L)*, 5(2):3019–3026, 2020.

[18] Leslie Pack Kaelbling, Michael L Littman, and Anthony R Cassandra. Planning and acting in partially observable stochastic domains. *Artificial intelligence*, 101(1-2):99–134, 1998.

[19] Moo Jin Kim, Karl Pertsch, Siddharth Karamcheti, Ted Xiao, Ashwin Balakrishna, Suraj Nair, Rafael Rafailov, Ethan Foster, Grace Lam, Pannag Sanketi, et al. Openvla: An open-source vision-language-action model. *arXiv preprint arXiv:2406.09246*, 2024.

[20] Mykel J Kochenderfer. *Decision making under uncertainty: theory and application*. MIT press, 2015.

[21] Joonho Lee, Jemin Hwangbo, Lorenz Wellhausen, Vladlen Koltun, and Marco Hutter. Learning quadrupedal locomotion over challenging terrain. *Science robotics*, 5(47):eabc5986, 2020.

[22] Kimin Lee, Younggyo Seo, Seunghyun Lee, Honglak Lee, and Jinwoo Shin. Context-aware dynamics model for generalization in model-based reinforcement learning. In *International Conference on Machine Learning*, pages 5757–5766. PMLR, 2020.

[23] Jens Lehmann, Robert Isele, Max Jakob, Anja Jentzsch, Dimitris Kontokostas, Pablo N Mendes, Sebastian Hellmann, Mohamed Morsey, Patrick Van Kleef, Sören Auer, et al. Dbpedia—a large-scale, multilingual knowledge base extracted from wikipedia. *Semantic web*, 6(2):167–195, 2015.

[24] Shilong Liu, Zhaoyang Zeng, Tianhe Ren, Feng Li, Hao Zhang, Jie Yang, Qing Jiang, Chunyuan Li, Jianwei Yang, Hang Su, et al. Grounding dino: Marrying dino with grounded pre-training for open-set object detection. In *European Conference on Computer Vision*, pages 38–55. Springer, 2024.

[25] Wolfgang Maass. Neural nets with superlinear vc-dimension. *Neural Computation*, 6(5):877–884, 1994.

[26] Viktor Makoviychuk, Lukasz Wawrzyniak, Yunrong Guo, Michelle Lu, Kier Storey, Miles Macklin, David Hoeller, Nikita Rudin, Arthur Allshire, Ankur Handa, et al. Isaac gym: High performance gpu-based physics simulation for robot learning. *arXiv preprint arXiv:2108.10470*, 2021.

[27] Leonor Michaelis, Maud L Menten, et al. Die kinetik der invertinwirkung. *Biochem. z.*, 49(333-369):352, 1913.

[28] Mayank Mittal, Calvin Yu, Qinxi Yu, Jingzhou Liu, Nikita Rudin, David Hoeller, Jia Lin Yuan, Ritvik Singh, Yunrong Guo, Hammad Mazhar, et al. Orbit: A unified simulation framework for interactive robot learning environments. *IEEE Robotics and Automation Letters*, 8(6):3740–3747, 2023.

[29] Yao Mu, Tianxing Chen, Shijia Peng, Zanxin Chen, Zeyu Gao, Yude Zou, Lunkai Lin, Zhiqiang Xie, and Ping Luo. Robotwin: Dual-arm robot benchmark with generative digital twins (early version). *arXiv preprint arXiv:2409.02920*, 2024.

[30] Hannes Mühleisen and Christian Bizer. Web data commons-extracting structured data from two large web corpora. *LDOW*, 937(133-145):65, 2012.

[31] Suraj Nair, Aravind Rajeswaran, Vikash Kumar, Chelsea Finn, and Abhinav Gupta. R3m: A universal visual representation for robot manipulation. In *Conference on Robot Learning*, pages 892–909. PMLR, 2023.

[32] Abhishek Padalkar, Acorn Pooley, Ajinkya Jain, Alex Bewley, Alex Herzog, Alex Irpan, Alexander Khazatsky, Anant Rai, Anikait Singh, Anthony Brohan, et al. Open x-embodiment: Robotic learning datasets and rt-x models. *arXiv preprint arXiv:2310.08864*, 2023.

[33] Xue Bin Peng, Marcin Andrychowicz, Wojciech Zaremba, and Pieter Abbeel. Sim-to-real transfer of robotic control with dynamics randomization. In *2018 IEEE international conference on robotics and automation (ICRA)*, pages 3803–3810. IEEE, 2018.

[34] Ilija Radosavovic, Tete Xiao, Bike Zhang, Trevor Darrell, Jitendra Malik, and Koushil Sreenath. Real-world humanoid locomotion with reinforcement learning. *Science Robotics*, 9(89):eadi9579, 2024.

[35] John Schulman, Filip Wolski, Prafulla Dhariwal, Alec Radford, and Oleg Klimov. Proximal policy optimization algorithms. *arXiv preprint arXiv:1707.06347*, 2017.

[36] Shai Shalev-Shwartz and Shai Ben-David. *Understanding machine learning: From theory to algorithms*. Cambridge university press, 2014.

[37] Mohit Shridhar, Lucas Manuelli, and Dieter Fox. Cliport: What and where pathways for robotic manipulation. In *Conference on robot learning*, pages 894–906. PMLR, 2022.

[38] Mohit Shridhar, Lucas Manuelli, and Dieter Fox. Perceiver-actor: A multi-task transformer for robotic manipulation. In *Conference on Robot Learning*, pages 785–799. PMLR, 2023.

[39] Eduardo D Sontag et al. Vc dimension of neural networks. *NATO ASI Series F Computer and Systems Sciences*, 168:69–96, 1998.

[40] Nitish Srivastava, Geoffrey Hinton, Alex Krizhevsky, Ilya Sutskever, and Ruslan Salakhutdinov. Dropout: a simple way to prevent neural networks from overfitting. *The journal of machine learning research*, 15(1):1929–1958, 2014.

[41] Hengkai Tan, Songming Liu, Kai Ma, Chengyang Ying, Xingxing Zhang, Hang Su, and Jun Zhu. Fourier controller networks for real-time decision-making in embodied learning. In *Forty-first International Conference on Machine Learning*, 2024.

[42] Josh Tobin, Rachel Fong, Alex Ray, Jonas Schneider, Wojciech Zaremba, and Pieter Abbeel. Domain randomization for transferring deep neural networks from simulation to the real world. In *2017 IEEE/RSJ international conference on intelligent robots and systems (IROS)*, pages 23–30. IEEE, 2017.

[43] Emanuel Todorov, Tom Erez, and Yuval Tassa. Mujoco: A physics engine for model-based control. In *2012 IEEE/RSJ international conference on intelligent robots and systems*, pages 5026–5033. IEEE, 2012.

[44] An Dinh Vuong, Minh Nhat Vu, Hieu Le, Baoru Huang, Huynh Thi Thanh Binh, Thieu Vo, Andreas Kugi, and Anh Nguyen. Grasp-anything: Large-scale grasp dataset from foundation models. In *2024 IEEE International Conference on Robotics and Automation (ICRA)*, pages 14030–14037. IEEE, 2024.

[45] Tobias Weyand, Andre Araujo, Bingyi Cao, and Jack Sim. Google landmarks dataset v2-a large-scale benchmark for instance-level recognition and retrieval. In *Proceedings of the IEEE/CVF conference on computer vision and pattern recognition*, pages 2575–2584, 2020.

[46] Baoyuan Wu, Weidong Chen, Yanbo Fan, Yong Zhang, Jinlong Hou, Jie Liu, and Tong Zhang. Tencent ml-images: A large-scale multi-label image database for visual representation learning. *IEEE access*, 7:172683–172693, 2019.

[47] Fan Xie, Alexander Chowdhury, M De Paolis Kaluza, Linfeng Zhao, Lawson Wong, and Rose Yu. Deep imitation learning for bimanual robotic manipulation. *Advances in neural information processing systems*, 33:2327–2337, 2020.

- [48] Chengyang Ying, Zhongkai Hao, Xinning Zhou, Hang Su, Songming Liu, Dong Yan, and Jun Zhu. Task aware dreamer for task generalization in reinforcement learning. *arXiv preprint arXiv:2303.05092*, 2023.
- [49] Chengyang Ying, Hao Zhongkai, Xinning Zhou, Xuezhou Xu, Hang Su, Xingxing Zhang, and Jun Zhu. Peac: Unsupervised pre-training for cross-embodiment reinforcement learning. *Advances in Neural Information Processing Systems*, 37:54632–54669, 2024.
- [50] Zhecheng Yuan, Tianming Wei, Shuiqi Cheng, Gu Zhang, Yuanpei Chen, and Huazhe Xu. Learning to manipulate anywhere: A visual generalizable framework for reinforcement learning. *arXiv preprint arXiv:2407.15815*, 2024.
- [51] Tony Z Zhao, Vikash Kumar, Sergey Levine, and Chelsea Finn. Learning fine-grained bimanual manipulation with low-cost hardware. *arXiv preprint arXiv:2304.13705*, 2023.
- [52] Ziwen Zhuang, Zipeng Fu, Jianren Wang, Christopher G Atkeson, Sören Schwertfeger, Chelsea Finn, and Hang Zhao. Robot parkour learning. In *Conference on Robot Learning*, pages 73–92. PMLR, 2023.
- [53] Brianna Zitkovich, Tianhe Yu, Sichun Xu, Peng Xu, Ted Xiao, Fei Xia, Jialin Wu, Paul Wohlhart, Stefan Welker, Ayzaan Wahid, et al. Rt-2: Vision-language-action models transfer web knowledge to robotic control. In *Conference on Robot Learning*, pages 2165–2183. PMLR, 2023.

A Proofs

A.1 Details and Proof of the Lemma 3.1

We follow the setting in [8]. First, assume the hypothesis set of policies to grasp a fixed single point is \mathcal{H} and its VC dimension is d . When considering T tasks, each represented by a different grasping position, we take the k -shared task classifier (\mathcal{H}_k, g) [8]. Here $\mathcal{H}_k = \{h_1, \dots, h_k\} \subseteq \mathcal{H}$ is a subset of \mathcal{H} and g maps each task $t \in \mathcal{T}$ to some $h_t \in \mathcal{H}_k$. Thus the k -shared task classifier hypothesis is defined as $\mathcal{F}_{\mathcal{H},k} = \{f_{\mathcal{H}_k,g} : |\mathcal{H}_k| = k, \mathcal{H}_k \subseteq \mathcal{H}, g : \mathcal{T} \rightarrow K\}$, here $f_{\mathcal{H}_k,g}(\cdot, t) = h_{g(t)}(\cdot)$. Then [8] has shown that the VC dimension of $\mathcal{F}_{\mathcal{H},k}$ is at most $\mathcal{O}(T \log k + kd \log(Tkd))$.

As we consider \mathcal{H} as the set of neural networks, previous works have shown that the VC dimension of multi-layer neural networks is around the parameters of the neural networks [25, 39]. Thus $d \gg T$ in our setting and $\mathcal{O}(T \log k + kd \log(Tkd)) \approx \mathcal{O}(kd \log(Tkd))$.

Finally, we consider the task number T . Assume that grasping two points of which the distance below ϵ is similar, we need around $b^3 / \frac{4}{3}\pi\epsilon^3$ points for covering the grasping cube with size $b \times b \times b$. Thus, the VC dimension is at most

$$\begin{aligned} \mathcal{O}(kd \log(Tkd)) &= \mathcal{O}(kd \log(\frac{b^3}{\frac{4}{3}\pi\epsilon^3}kd)) \\ &= \mathcal{O}(kd \log(\frac{3b^3kd}{4\pi\epsilon^3})). \end{aligned} \tag{4}$$

A.2 Proof of the Lemma 3.2

Proof. Firstly, we convert normalized coordinates to pixel coordinates:

$$\begin{aligned} u_{i\min(\text{pixel})} &= u_{i\min} \times W_i \\ v_{i\min(\text{pixel})} &= v_{i\min} \times H_i \\ u_{i\max(\text{pixel})} &= u_{i\max} \times W_i \\ v_{i\max(\text{pixel})} &= v_{i\max} \times H_i \end{aligned}$$

Then, we compute the center of the bounding box in pixel coordinates:

$$\begin{aligned} u_{i\text{center}} &= \frac{u_{i\min(\text{pixel})} + u_{i\max(\text{pixel})}}{2} \\ v_{i\text{center}} &= \frac{v_{i\min(\text{pixel})} + v_{i\max(\text{pixel})}}{2} \end{aligned}$$

These points represent the projections of the sphere's center onto the image planes.

Secondly, for each camera, we back-project the center point into a 3D viewing ray in camera coordinates:

$$\mathbf{d}_i = K_i^{-1} \begin{bmatrix} u_{i\text{center}} \\ v_{i\text{center}} \\ 1 \end{bmatrix}$$

This gives the direction vector \mathbf{d}_i in the camera coordinate system.

Therefore, we can express the sphere center in camera coordinates since the sphere's center lies somewhere along the viewing ray:

$$\mathbf{C}_{i,\text{cam}} = \lambda_i \mathbf{d}_i$$

where $\lambda_i > 0$ is an unknown scalar representing the distance along the ray from the camera center to the sphere's center.

Thirdly, we transform the sphere center from camera coordinates to world coordinates:

$$\mathbf{C} = R_i^\top \mathbf{C}_{i,\text{cam}} + \mathbf{t}_i = R_i^\top (\lambda_i \mathbf{d}_i) + \mathbf{t}_i$$

This must hold true for both cameras:

$$\mathbf{C} = R_1^\top (\lambda_1 \mathbf{d}_1) + \mathbf{t}_1 = R_2^\top (\lambda_2 \mathbf{d}_2) + \mathbf{t}_2$$

By equating the expressions for \mathbf{C} we get:

$$R_1^\top(\lambda_1 \mathbf{d}_1) + \mathbf{t}_1 = R_2^\top(\lambda_2 \mathbf{d}_2) + \mathbf{t}_2$$

By rewriting we have:

$$R_1^\top \mathbf{d}_1 \lambda_1 - R_2^\top \mathbf{d}_2 \lambda_2 = \mathbf{t}_2 - \mathbf{t}_1$$

Let's denote:

$$\mathbf{a}_1 = R_1^\top \mathbf{d}_1$$

$$\mathbf{a}_2 = R_2^\top \mathbf{d}_2$$

$$\mathbf{b} = \mathbf{t}_2 - \mathbf{t}_1$$

So the equation becomes:

$$\mathbf{a}_1 \lambda_1 - \mathbf{a}_2 \lambda_2 = \mathbf{b}$$

Note that this is a system of three linear equations with two unknowns λ_1 and λ_2 :

$$\begin{cases} a_{1x}\lambda_1 - a_{2x}\lambda_2 = b_x \\ a_{1y}\lambda_1 - a_{2y}\lambda_2 = b_y \\ a_{1z}\lambda_1 - a_{2z}\lambda_2 = b_z \end{cases}$$

Since we have more equations than unknowns (overdetermined system), we can solve for λ_1 and λ_2 using least squares estimation.

Note that this can be written in matrix form:

$$\begin{bmatrix} a_{1x} & -a_{2x} \\ a_{1y} & -a_{2y} \\ a_{1z} & -a_{2z} \end{bmatrix} \begin{bmatrix} \lambda_1 \\ \lambda_2 \end{bmatrix} = \begin{bmatrix} b_x \\ b_y \\ b_z \end{bmatrix}$$

Let A be the 3×2 matrix of coefficients, λ the vector of unknowns, and \mathbf{b} the vector of constants:

$$A = \begin{bmatrix} a_{1x} & -a_{2x} \\ a_{1y} & -a_{2y} \\ a_{1z} & -a_{2z} \end{bmatrix}, \quad \lambda = \begin{bmatrix} \lambda_1 \\ \lambda_2 \end{bmatrix}, \quad \mathbf{b} = \begin{bmatrix} b_x \\ b_y \\ b_z \end{bmatrix}$$

We can compute the least squares solution:

$$\lambda = (A^\top A)^{-1} A^\top \mathbf{b}$$

Once λ_1 and λ_2 are found, **C can be calculated using either camera's equation:**

$$\mathbf{C} = R_1^\top(\lambda_1 \mathbf{d}_1) + \mathbf{t}_1$$

Alternatively, we compute both and average them for robustness:

$$\mathbf{C} = \frac{1}{2} (R_1^\top(\lambda_1 \mathbf{d}_1) + \mathbf{t}_1 + R_2^\top(\lambda_2 \mathbf{d}_2) + \mathbf{t}_2)$$

Finally, since λ_i and λ_2 are found, we can compute the distance Z_i from the camera along the viewing direction \mathbf{d}_i :

$$\mathbf{C}_{i,\text{cam}} = \lambda_i \mathbf{d}_i = Z_i \cdot \hat{\mathbf{d}}_i$$

where $\hat{\mathbf{d}}_i$ is normalized by:

$$\hat{\mathbf{d}}_i = \frac{\mathbf{d}_i}{\|\mathbf{d}_i\|}$$

The projected radius of the sphere s_i (in pixels) is half the size of the bounding box width or height (assuming the sphere projects to a circle):

$$s_i = \frac{w_i + h_i}{4}$$

where

$$w_i = u_{i\text{max(pixel)}} - u_{i\text{min(pixel)}}$$

$$h_i = v_{i\text{max(pixel)}} - v_{i\text{min(pixel)}}$$

Consider similar triangles in the imaging geometry:

$$\frac{s_i}{f_i} = \frac{r}{Z_i}$$

We can compute the radius of the sphere:

$$r = \frac{s_i \cdot Z_i}{f_i}$$

Additionally, the solution is unique provided that:

- **The Cameras Are Not Aligned:** The direction vectors \mathbf{a}_1 and \mathbf{a}_2 are not colinear.
- **Non-Degenerate Configuration:** The cameras have different positions or orientations, ensuring the lines of sight intersect at a single point.

Under these conditions, the least squares solution yields a unique λ , and thus unique \mathbf{C} and r .

□

B Ablation Study

To demonstrate the essential role of 3D spatial and 1D temporal information for spatial intelligence, we perform an additional experiment focusing on **temporal variability**, in addition to the spatial generalization tests in Sec. 4. This experiment includes an ablation study comparing models trained on a few selected key timesteps with those trained on all timesteps in a full trajectory. To further illustrate the robust inference capabilities achieved by the enhanced **policy generalization**, we test the policy’s ability to handle significant uncertainty in the output of the visual model. During inference, we apply random masks and noise to the visual model’s bounding box outputs, allowing us to evaluate the policy’s generalization ability under such conditions.

B.1 Training with Only Key Steps.

To assess the impact of temporal information on policy effectiveness, we conduct an experiment where the model is trained using only key steps from the trajectory. The specific key steps selected were [0, 18, 20, 22, 70], chosen to represent pivotal moments in the trajectory for the grasping task: 0 corresponds to the initial state before the gripper starts approaching the apple, 70 represents the final state when the robotic arm retracts, and steps 18 to 22 denote intermediate states where the gripper makes contact with the apple and closes around it.

Table 3: Success Rates for Training with Only Key Steps

Experiment	Real Robot SR	Simulation SR
Training with Full Trajectory	90%	81.25%
Training with Key Steps	0%	4.17%

The results in Tab. 3 indicate a stark difference in performance between training with the full trajectory and training with only key steps. Training with the full trajectory resulted in a success rate of 90% on the real robot and 81.25% in simulation. In contrast, training with only key steps leads to complete failure on the real robot (0% success rate) and a significantly reduced success rate of 4.17% in simulation. This outcome highlights that relying solely on key steps fails to provide the temporal continuity necessary for effective spatial generalization. The policy’s inability to capture sufficient context from isolated states results in poor action generation and overall task failure.

B.2 Robustness against Detection Failure during Inference.

During the inference phase, visual models such as YOLO-World may not always successfully identify objects, leading to significant uncertainty in visual input.



Figure 6: A case of detection failure. The task is to catch apples to a specified location in a normal environment.



Figure 7: A case of detection failure. The task is to catch apples at a specified location in a flittering light environment.

Our policy still works well in situations where the visual model fails to detect. For example, visual models may fail to detect target objects when the robotic arm approaches the target, under dim lighting conditions, or when there is partial occlusion of the target by the background (see Figures 6 and 7). Especially, when using flickering and swaying point light sources in dimly lit environments, the detection by visual models is particularly unstable. Such failures may occur at any timestep during manipulation and may persist for several timesteps. Moreover, these failures are unstable and unpredictable. For the same object placement, the occurrence of detection failures during manipulation does not consistently happen or not happen at the same timestep.

Despite all those failures and instabilities in detecting bounding boxes, our model can still successfully and accurately accomplish the manipulation tasks.

To test our policy’s robustness against this visual uncertainty, we introduce masks that randomly obscured bounding box input at varying ratios (0.0 to 1.0) during inference.

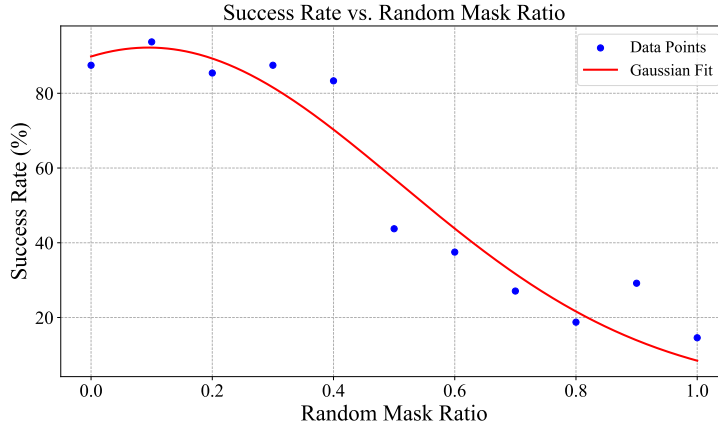


Figure 8: The relationship between random mask ratio and success rate. The fitted curve represents a Gaussian function of $y = 92.23 \exp\left(-\frac{(x-0.09)^2}{2 \cdot 0.41^2}\right)$.

As shown in Fig. 8, the results reveal that the policy maintains a high success rate and generalization capability when the mask ratio is below 0.4. As the mask ratio exceeds 0.4, the success rate significantly declines, leading to consistent policy failures. Coincidentally, the random mask ratio we add in the student policy training phase is 0.3. This trend reveals that our approach focusing on policy generalizability can resist visual uncertainty up to 40% of the masking ratio. That is, even if 40% of the visual information is lost, the policy still has good spatial generalizability. We fitted the data points with a Gaussian curve to represent this trend, defined by the equation:

$$y(x) = a \cdot e^{-\frac{(x-b)^2}{2c^2}} \quad (5)$$

where a , b , and c are parameters that define the height, center, and width of the curve, respectively. This curve demonstrates that the policy is resilient up to moderate levels of visual masking (mask ratios up to 0.3), but performance degrades significantly as the masking ratio increases beyond 0.4.

This experiment validates that our policy can withstand moderate visual uncertainties during inference, maintaining robust performance. This shows that our focus on policy generalization can easily cope with situations where the visual model has large uncertainty, leading to more robust manipulation. However, the steep decline in success rate for higher mask ratios highlights the importance of reliable visual input for effective spatial reasoning and task execution.

As to whether the random mask in the training phase gives some increase in the success rate of our policy, please refer to Sec. B.3.

B.3 Random Mask during Student Policy Training Affects Performance.

The uncertainty of visual detection in the real world is mentioned in the previous subsection, in order to demonstrate that random masking during training does favor the performance of the student policy. Specifically, we compare the success rates of policies trained with and without a random mask ratio of 0.3 across five different spatial ranges. During training, we randomly mask out 0 to 30% of the bounding box information in each trajectory. This encourages the policy to adapt to scenarios where bounding box detection is incomplete or inaccurate. Table 4 demonstrated that in all range of spaces, the policy trained with random masks shows outstanding performance compared with one without masks. In addition, the policy shows better robustness in larger spatial ranges, where the variability and uncertainty of detection are more pronounced, highlighting the effectiveness of random masking in improving spatial adaptability and generalization.

Table 4: Comparison of Success Rates With and Without Random Mask

Spatial Range	Random Mask Ratio = 0.3	Without Random Mask
Fix Point	100.0%	100.0%
5 cm × 5 cm × 5 cm	83.33%	79.17%
10 cm × 10 cm × 10 cm	97.92%	64.58%
20 cm × 20 cm × 20 cm	87.5%	70.83%
Full Space (41 cm × 30 cm × 28 cm)	87.5%	68.75%

B.4 Random Noise in Bounding Boxes during Inference.

To further examine the policy’s robustness against visual uncertainty, we introduce random noise to the bounding boxes during inference. We tested noise ratios at increments of 0.01, 0.02, 0.05, 0.1, 0.2, and 0.5. Fig. 9 illustrates the success rate as a function of noise ratio, where a monotonic decay fit highlights the policy’s performance trend. The results show that the policy maintains a high success rate at low noise ratios but experienced a significant decrease as noise levels increased. Since our normalized bounding box value ranges from 0 to 1, the policy still achieves a high success rate with a visual detection error of 0.05, demonstrating the robustness of the policy generalization to cope with visual uncertainty and visual Sim2Real gap.

Our experiments highlight that achieving spatial intelligence requires both continuous temporal information and sufficient spatial data. The experiments in our main text demonstrate that spatial generalizability requires sufficient spatially varying data. The first ablation experiment shows that continuous temporal context is crucial for effective policy performance, while the second and third ablation experiments demonstrate that policy generalization can cope with notable visual uncertainty.

B.5 Comparison with IK and Other Baselines in the Simulator

In order to demonstrate the robustness of our method compared to other baseline methods on the grasping task, we compare our method to a heuristics-based approach, in particular the Inverse Kinematics (IK) algorithm from Isaac Lab which is required in some heuristics-based approaches

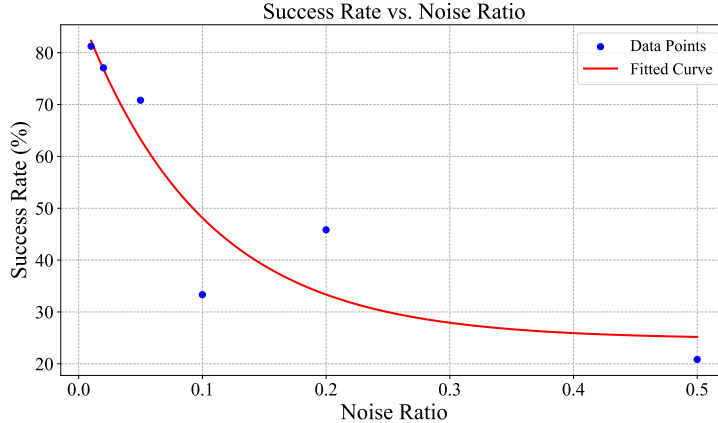


Figure 9: The relationship between noise ratio and success rate. The fitted curve represents a exponential function of $y = 63.62 \exp(10.01x) + 24.75$.

such as AnyGrasp [9]. We conduct tests using 3 different seeds in the simulator, and the comparison results are as follows:

- **Inverse Kinematics (IK):** This approach directly uses the ground truth object pose as the target end-effector (eef) pose, then computes the joint positions via IK to move the robot arm to the target. However, we observe that IK performs poorly at the edges of the workspace, especially when objects are near the table surface or at low positions. Examples of IK failures when the table is very low can be seen in Fig. 10 and Fig. 11. An example of an IK success can be seen in Fig. 12. The reason for IK failures is possible:
 - The robotic arm may approach singular configurations where the Jacobian matrix becomes singular, causing unstable or undefined IK solutions.
 - Near the workspace edge, numerical inaccuracies may result in imprecise IK solutions. Moreover, approximation methods (e.g., pseudoinverse) may struggle to converge to a valid solution in complex boundary cases.
- **Key Steps:** In this approach, only key steps of the trajectory are used to model the grasping task.
- **Without Random Mask:** This variant trains the student policy without random masking for object positioning.

Here, we get some key insights:

- **IK Limitations:** As expected, IK struggles in the workspace boundaries due to singularities, which cause failures when the object is positioned at the edges of the table or at low heights. This limitation is inherent to traditional geometric methods like IK, which rely on precise pose knowledge and are prone to errors in challenging environments.
- **Our RL-Based Approach:** In contrast, **ManiBox (Ours)** utilizes RL to learn robust grasping teacher policies by directly planning the joint positions, enabling successful manipulation across a wide range of object positions. Our method does not rely on explicit pose knowledge and is highly effective even at challenging object locations that cause IK to fail.



Figure 10: An example of IK failure (view of the center camera): the object is at the edge of the robotic arm’s workspace - a case where the object height is too low.



Figure 11: An example of IK failure (view of the left camera): the object is at the edge of the robotic arm’s workspace - a case where the object height is too low.

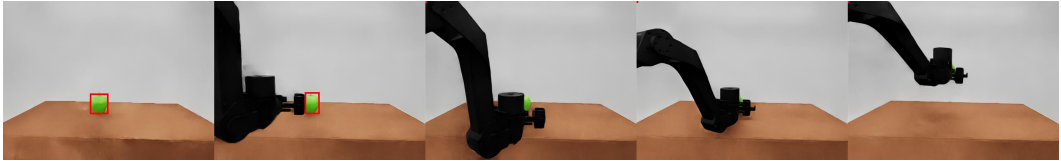


Figure 12: An example of an IK success.

C More Real-World Experiments

To demonstrate the extensibility of our approach, we supplement more real-world experiments: **Mid-Air** (Figure 13) and **Cluttered Table** at varying heights (Figure 14 and Figure 15).



Figure 13: **Task: Mid-Air.** Grasp the bottle lifted by hand and suspended in mid-air, then move it to the target position.

D More Simulation Experiments

In addition to single-object grasping, we also examine the spatial scaling law for the dual-object pouring task. In this context, spatial volume is defined as the spatial range within which each object is randomly positioned. However, to prevent collisions, the spatial ranges of the two objects are designed to be non-overlapping. Due to the involvement of two objects and their spatial interactions and different spatial position ranges in the pouring task, potential spatial conflicts may arise between the randomly positioned objects, leading to discrepancies between the scaling curves of pouring and grasping. To address this, we employ a right-shifted Michaelis-Menten curve to optimally fit the scaling relationship between spatial generalization and data volume, as shown in Fig. 16. Given the aforementioned task differences and the presence of noise in the experimental data, the power-law relationship between spatial volume and data amounts needed to reach 80% grasping success rate is presented in Fig. 17.

E Experimental Details

We test the success rate of student policy in both simulator and real world.

E.1 Evaluation in Simulation

We run large-scale experiments in the simulator to test the spatial generalization curve for each range and determine the minimum data amounts to achieve an optimal success rate. To align with real robot inference, we set the robot’s joints directly to target qpos instead of using environment stepping. We mark the trajectory as success if there is a step both reaching reward > 0.6 and quat reward > 1.4 . For each policy, we test 48 trajectories and record the final success rate. The experiment consists of



Figure 14: **Task: Cluttered Table.** Grasp the apple from a cluttered table with a height of 60 cm.



Figure 15: **Task: Cluttered Table.** Grasp the apple from a cluttered table with a height of 74.5 cm.

three rounds of tests with different seeds, each with 16 trajectories. In each round, the target random points are sampled from a uniform distribution.

E.2 Experiment Result Analysis

We discuss our spatial scaling law here

$$\text{data_volume} = 640.32 \cdot \text{spatial_volume}^{0.35} \quad (6)$$

By fitting the resulting data points, we observe that as the training data increases, the success rate of the policies quickly rises and eventually converges to an upper bound, which aligns well with the form of the Michaelis-Menten [27] equation:

$$\text{success_rate} = \frac{V_{\max} \times \text{num_traj}}{K_m + \text{num_traj}} \quad (7)$$

where V_{\max} represents the maximum achievable success rate, and K_m is the number of trajectories at which the success rate is half of V_{\max} . This equation captures the saturation-type growth observed in the policy performance.

For the functional relationship between the amount of data required for spatial generalization and spatial volume, we explored two types of fits: a power law and a logarithmic function. The fitting results of power law is given by $y = a \cdot x^b = 640.32x^{0.35}$, while the logarithmic fit is $y = a \cdot \ln(b \cdot x) + c = 2095.51 \cdot \ln(0.3 \cdot x) - 642.93$. We found that the logarithmic fit becomes unreasonable as the spatial volume x approaches 0, where the required data, $y = a \cdot \ln(b \cdot x) + c = 2095.51 \cdot \ln(0.3 \cdot x) - 642.93$, tends to negative infinity, which is unrealistic since the amount of data cannot be negative. Furthermore, the fit results in a negative value at $x = 3.3$, where $bx = 1$ and $\log(bx) = 0$, leading to a required data amount of $a \log(bx) + c = -642.93$. In the long run (for larger spatial volumes), the power law fit better describes the relationship between the data required for spatial generalization and spatial volume. Fig. 18 shows the selected power law relationship, and Fig. 19 displays the logarithmic curve.

E.3 Evaluation in Real World

E.3.1 Real-World Success Rate

To verify our experiment results from the simulator, we evaluate our policy in the real robot. For each range, we choose the first optimal policy that achieves 80% success rate in simulator and evaluate with the real robot for 10 randomly chosen points.

Random Placement of Objects in Real-world Evaluation. To be more specific, we divide the maximum range, namely the full space ($41\text{cm} \times 30\text{cm} \times 28\text{cm}$), into three equal parts in height, two equal parts in width, and three equal parts in length, resulting in a total of $3 \times 2 \times 3 = 18$ equally sized spatial cuboid ranges at different positions. For each tested spatial range, ten different points are uniformly selected to test the robot’s manipulation success rate.

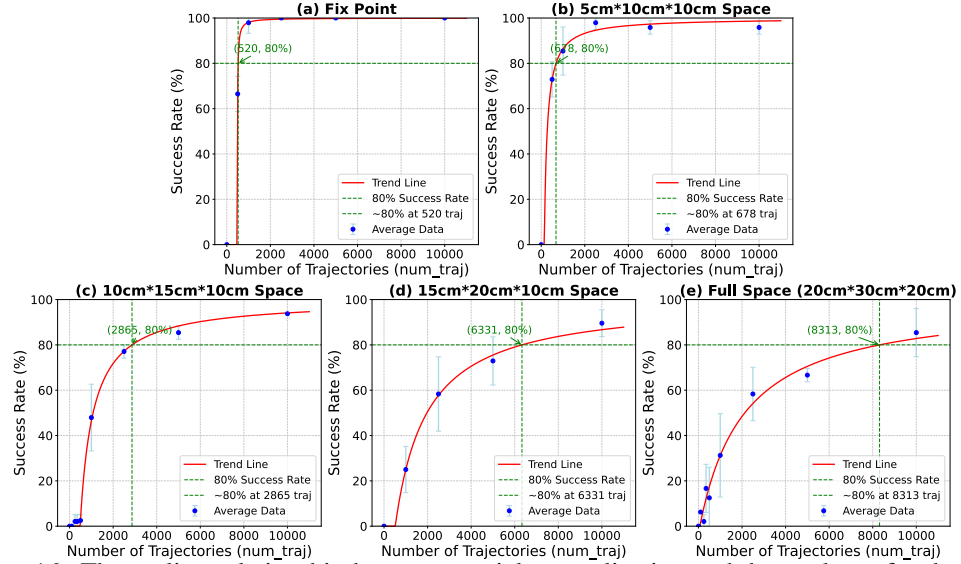


Figure 16: The scaling relationship between spatial generalization and data volume for the task of pouring water, measured under different spatial ranges. Data volume represents the number of trajectories used to train the student policy. The estimated 80% success point is marked, with blue points showing the average success rate across 3 seeds and error bars indicating standard deviation.

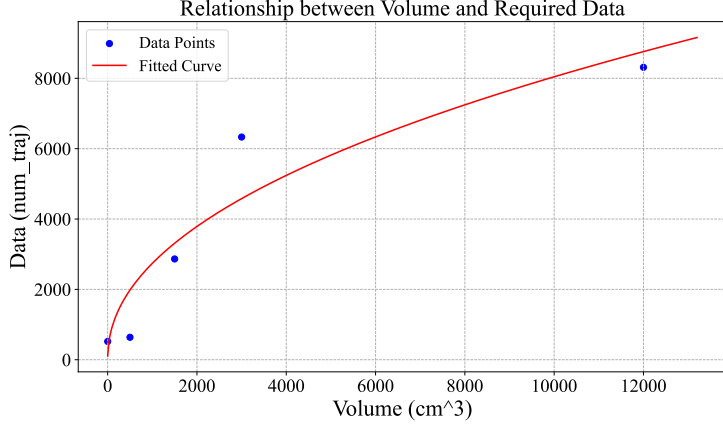


Figure 17: The relationship between spatial volume and data amounts needed to reach 80% grasping success rate. The fitted curve represents a power function $y = 108.24 \cdot x^{0.48}$.

E.3.2 Real-World Experiment Settings

To verify our methods, we evaluate the student policy in the real robot, which is trained on simulation data of full space (41cm * 30cm * 28cm) with the real robot.

Spatial Generalization. As illustrated in Fig. 4, we divide the spatial range horizontally into Left (L), Right (R), and Center (C), and vertically into Front (F) and Back (B), and randomly select points within these sections on different heights to test our policy³. All these points are arbitrarily selected, which means that the target object has an equal chance of appearing at the center or the edge of the table, far from or close to the robot, in positions that require the robotic arm to reach upwards or downwards. We hope this approach reflects the spatial generalization of our policy comprehensively and honestly.

In addition to the verification of spatial generalization, we also test the ability of Object generalization and background generalization. The details of the experiment setting can be found in Tab. 5.

³The table is an elevated table and can therefore be adjusted to any height.

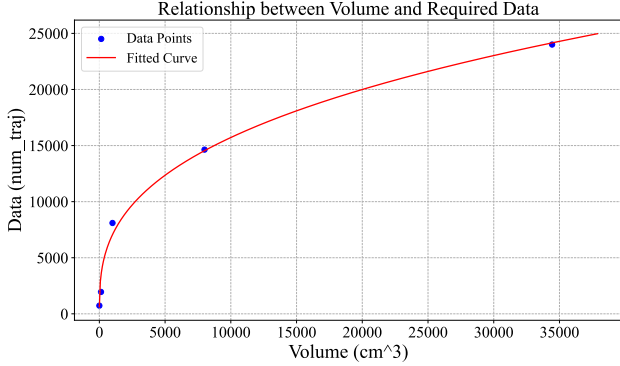


Figure 18: Demonstration of the power-rate relationship between spatial volume and data amounts needed to reach 80% success rate in the grasping task.

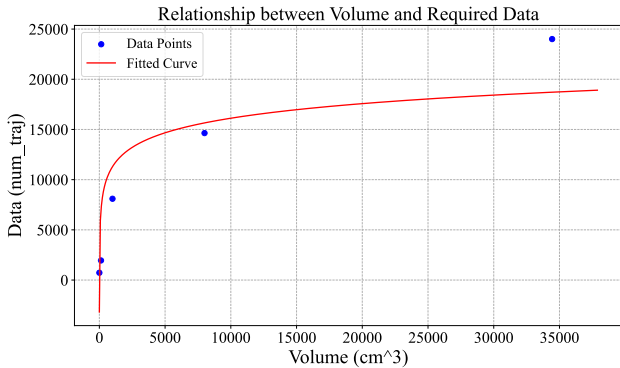


Figure 19: Demonstration of the logarithmic relationship between spatial volume and data amounts needed to reach 80% success rate in the grasping task.

Object Generalization and Background Generalization. Furthermore, we have chosen objects of various shapes, sizes, and materials as target objects for testing, all of which were previously unseen by our policy. To be more specific, during training, we only encountered apples with sizes of approximately (6.9cm – 7.4cm, 6.9cm – 7.4cm, 6.9cm – 7.4cm) in the XYZ direction, while the test target objects span a size range of (5.1cm – 7.0cm, 5.1cm – 9.7cm, 6.0cm – 22.7cm) in the XYZ direction. Additionally, although apples are roughly spherical, the target objects also include cylindrical and pyriform shapes. Moreover, the target objects encompass different materials such as glass and metal. All these objects serve to demonstrate our policy’s capability to generalize to varying shapes, sizes, and materials.

The three camera images, as well as the entire trajectory of grasping, are schematized below in Figure 20:

Table 5: Real-World Experiment Settings. Note that we use only the bounding boxes of the objects for both student policy training and inference. Bolded object sizes are never seen in training.

Generalization Type	Object Size (cm) of XYZ	Setting Description
Object in Simulation Data		
Apple (Domain Randomization)	(6.9-7.4, 6.9-7.4, 6.9-7.4)	Distribute uniformly in a configurable spatial volume
Object Generalization		
Yellow Pear	(6.5, 5.5, 10.7)	h4: Point Random, Minimal setting
Orange	(7.0, 6.7, 6.5)	h4: Point Random, Minimal setting
Steel Cup	(6.5, 9.7, 10.8)	h4: Point Random, Minimal setting
Tin Can	(5.1, 5.1, 7.2)	h4: Point Random, Minimal setting
Glass Beaker	(5.1, 5.1, 6.0)	h4: Point Random, Minimal setting
Background Generalization		
Apple	(7.2, 7.4, 6.9)	h4: Point Random, Orange tablecloth
Unseen Apple	(7.0, 7.5, 7.0)	h4: Point Random, Black tablecloth
Apple	(7.2, 7.4, 6.9)	h4: Point Random, Playing video
Apple	(7.2, 7.4, 6.9)	h4: Point Random, Dim light
Apple	(7.2, 7.4, 6.9)	h4: Point Random, Flittering light
Complex Generalization		
Unseen Apple, Unseen Table	(7.0, 7.5, 7.0)	Point Random, Table 2
Unseen Apple, Unseen Desk	(7.0, 7.5, 7.0)	Point Random, Multiple objects
Steel Cup, Unseen Desk	(6.5, 9.7, 10.8)	Point Random, Daily desktop
Plastic Bottle, Unseen Desk	(6.4, 6.4, 22.27)	Point Random, Daily desktop

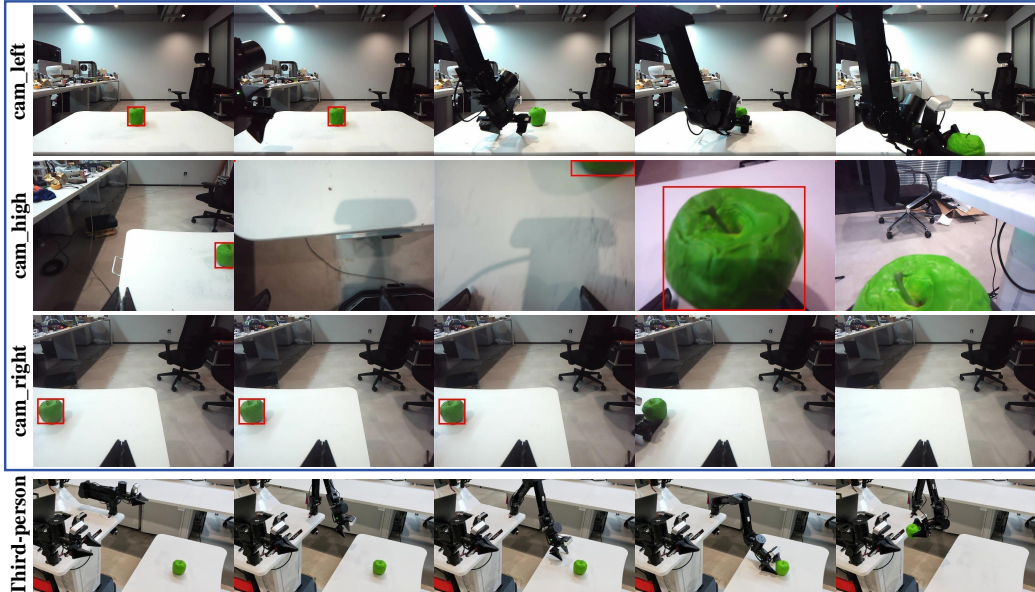


Figure 20: Pictures of the entire trajectory of grasping, including perspective and three camera views.

E.4 More Real-world Results

Table 6: The real-world success rate (SR) of Manibox and vision-based ACT under varied spatial volumes. We select an approximate data amount based on the results in Fig. 3a.

Spatial Range	Method	SR
Fixed Point	Vision-Based ACT	70%
	ManiBox (Ours)	100%
5cm*5cm*5cm	Vision-Based ACT	0%
	ManiBox (Ours)	70%
10cm*10cm*10cm	Vision-Based ACT	0%
	ManiBox (Ours)	100%
20cm*20cm*20cm	Vision-Based ACT	-
	ManiBox (Ours)	80%
Full Space (41cm*30cm*28cm)	Vision-Based ACT	-
	Vision-Based ACT (100 real-world data)	0%
	ManiBox (Ours)	90%

F Teacher-Student Training Details

For ease of understanding, Alg. 1 is the pseudo algorithm for the ManiBox method.

F.1 Teacher Policy Details

We train our teacher policy using PPO with 8,192 parallel environments in Isaac Lab [28]. With a carefully designed reward function and applied PPO techniques, the training is completed in around 40 minutes, reaching approximately 2,000 training iterations. The task involves training a robot to grasp an apple randomly placed on a liftable table and transport it to a designated target position (Figure 21).



Figure 21: The simulation environment consists of a room with a table, an apple, and a robot. The task is for the robot to grasp the apple and place it in a specified location.

The advantages of using a teacher policy instead of direct visual RL training can be summarized in three key aspects. First, the teacher policy relies solely on robot and object information as input, significantly reducing the dimensionality of the state space. Second, the incorporation of privileged information and tailored reward functions for critical steps offers more focused guidance during training, thereby narrowing the exploration space. Lastly, visual RL suffers from limited parallelizability, which results in lower overall training efficiency.

F.1.1 Simulation Scenario Setup

The environment is built based on the lift task in Isaac Lab. During training, the scene consists of a table, an apple, and a robot. The robot is initialized at a fixed starting position at the beginning of each episode. The apple's size, as well as its x,y position, are uniformly randomized across environments, while the height of the table is also uniformly randomized. The target position, however, remains fixed throughout all training episodes. Key steps captured from three camera perspectives are shown in Figures 22, 23, and 24. To support future extensions to more complex tasks, such as obstacle avoidance during grasping, we represent the robot's behavior with a 30Hz trajectory. Each environment in the simulator is evenly spaced to prevent interference between different training instances. Further details on the randomized ranges can be found in Table 7.

Algorithm 1 Training and Deployment Algorithm of ManiBox

Require: Simulator environment Sim , Real robot $Robot$
Require: Proximal Policy Optimization (PPO) for training teacher policy
Require: Bounding box extractor $BBoxExtractor$
Require: Maximum dataset size N_{max} , reward function R , domain randomization module DR

1: **Stage 1: Teacher Policy Training**
2: Initialize teacher policy π_β with random weights
3: Set Sim environment with reward function R and domain randomization module DR
4: **while** not converged **do**
5: Collect trajectory data \mathcal{D}_T in Sim using π_β
6: Update π_β using PPO with \mathcal{D}_T
7: **end while**

8: **Stage 2: Simulation Data Generation**
9: Initialize dataset $\mathcal{D}_S = \emptyset$
10: **while** $|\mathcal{D}_S| < N_{max}$ **do**
11: Reset Sim environment
12: Apply domain randomization DR to environment
13: Generate trajectory $\tau = \{(o_t^{rob}, a_t, r_t)\}_{t=1}^T$ using π_β
14: Extract bounding boxes $\{o_t^{vis}\}_{t=1}^T$ using $BBoxExtractor$
15: Store $\{(o_t^{vis}, o_t^{rob}, a_t)\}_{t=1}^T$ in \mathcal{D}_S
16: **end while**

17: **Stage 3: Student Policy Training**
18: Initialize student policy π_θ with random weights
19: **while** not converged **do**
20: Sample trajectory $\tau = \{(o_t^{vis}, o_t^{rob}, a_t)\}_{t=1}^T$ from \mathcal{D}_S
21: Randomly mask some o_t^{vis} to simulate detection failures
22: Update $\pi_\theta(o_{\leq t}^{vis}, o_{\leq t}^{rob})$ using the masked τ
23: **end while**

24: **Stage 4: Real-World Deployment**
25: $t \leftarrow 0$
26: **while** not terminated **do**
27: Extract real-world bounding boxes o_t^{vis} using $BBoxExtractor$
28: Compute action $a_t \sim \pi_\theta(o_{\leq t}^{vis}, o_{\leq t}^{rob})$
29: Execute action a_t on $Robot$
30: $t \leftarrow t + 1$
31: **end while**



Figure 22: Key steps of grasping in simulation in cam_high view.

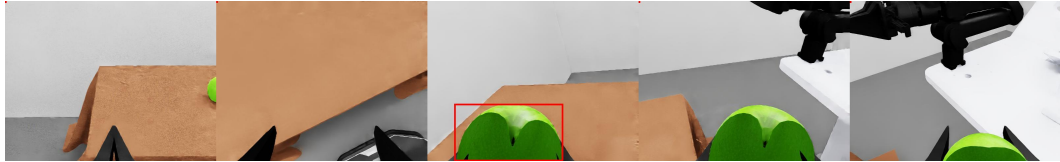


Figure 23: Key steps of grasping in simulation in cam_left_wrist view.

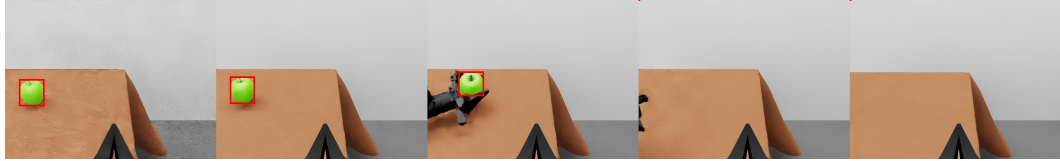


Figure 24: Key steps of grasping in simulation in cam_right_wrist view.

Table 7: Environment Randomization Parameters

Spatial Range	Table Height (z)	Apple X Position	Apple Y Position
Fix Point	(-0.00, 0.00)	(-0.0, 0.0)	(-0.0, 0.0)
5 cm × 5 cm × 5 cm	(-0.025, 0.025)	(-0.025, 0.025)	(-0.025, 0.025)
10 cm × 10 cm × 10 cm	(-0.07, 0.03)	(-0.05, 0.05)	(-0.05, 0.05)
20 cm × 20 cm × 20 cm	(-0.1, 0.1)	(-0.1, 0.1)	(-0.05, 0.15)
Full Space (41 cm × 30 cm × 28 cm)	(-0.13, 0.15)	(-0.22, 0.08)	(-0.05, 0.36)
Apple 3D Scale Range	((0.77, 0.82), (0.77, 0.82), (0.77, 0.82))		

F.1.2 Manipulation Tasks on Two Objects

Manipulation tasks involving two objects require the detection model to recognize the two objects and then perform the corresponding skills. And a policy is trained to master a specific manipulation skill, such as pouring, grasping, or placing. For example, the pouring policy recognizes two bounding boxes, “bottle” and “cup”, and then the policy will grab the bottle and pour it into the cup. Through the decoupling of the teacher policy and student policy, our approach offers significant flexibility in training the teacher policy. This flexibility allows for the utilization of both RL methods, as previously discussed, and alternative approaches such as state machines. Given the inherent challenges of training RL for multi-object, long-horizon manipulation tasks, ManiBox employs a state machine as the teacher policy specifically for the pouring water task. Notably, the remaining components of the system remain unchanged, ensuring consistency and reliability in the overall framework.

In the task of pouring water, the x,y positions of the bottle and cup are uniformly randomized across environments, while the height of the table is also uniformly randomized. Key steps captured in the simulator are shown in Fig. 25.



Figure 25: Key steps of pouring water in simulation in cam_high view.

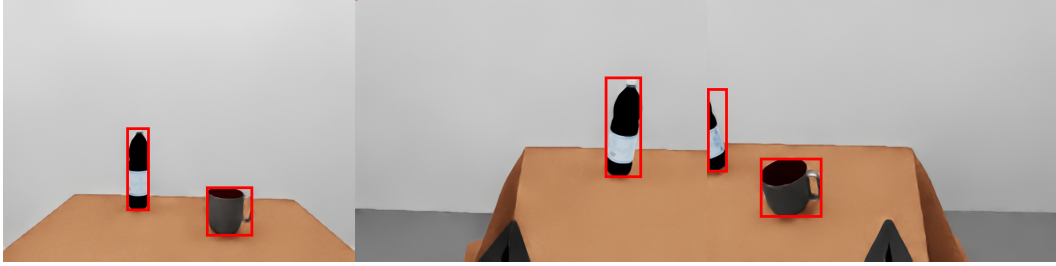


Figure 26: Three views of the initial timestep of the pouring water task, in order: cam_high, cam_left_wrists, and cam_right_wrists.

F.1.3 Details of Observation and Action

We provide detailed information about the observations and actions used in training the teacher policy for the multi-environment object-grasping manipulation task:

- **Observations:**
 - Contact forces (24-dimensional)
 - Joint position (8-dimensional)
 - Joint velocity (8-dimensional)
 - Object position (3-dimensional)
 - Target location (7-dimensional)
 - Last action (8-dimensional)
- **Actions:**
 - Joint Position (8-dimensional) (We choose position control. The action is the expected joint position for the next timestep.)

F.1.4 Implementation of PPO

Our PPO implementation is built on `rsl_rl`, and leverages several techniques to improve stability and performance. Key components and their settings are summarized in Table 8.

Table 8: PPO Parameters

Techniques	Parameter	Value
Clipped Surrogate Objective	clip_param	0.2
Value Function Clipping	use_clipped_value_loss	True
Value Loss Coefficient	value_loss_coef	1.0
Adaptive KL Penalty	desired_kl	0.01
Entropy Regularization	entropy_coef	0.01
Generalized Advantage Estimation (GAE)	gamma	0.99
	lam	0.95
Gradient Clipping	max_grad_norm	1.0
Learning Rate	learning_rate	0.001
Mini-Batch	num_mini_batches	4
Learning Epochs	num_learning_epochs	5
Schedule	schedule	adaptive
Empirical Normalization	empirical_normalization	True

F.1.5 Reward Function Design

To ensure that the policy achieves the desired grasping behavior on our robot, we design a reward function that reflects the task’s objectives. As grasping is complicated, it can be divided into a multi-stage reward function: first reaching the object, then closing the jaws, then picking up the object, and finally retracting the robotic arm to a specified position. Definitions of different part of our reward function for the specific object-grasp task are stated as follows:

- **Fingers Open**

$$R_{\text{fingers_open}} = \tanh\left(\frac{\|\mathbf{p}_{\text{object}} - \mathbf{p}_{\text{ee}}\|_2}{\sigma}\right) \cdot \sum_{i=1}^2 \text{finger_pos}[i]$$

where $\mathbf{p}_{\text{object}}$ represents the position of the object in world coordinates. \mathbf{p}_{ee} represents the position of the end-effector in world coordinates. finger_pos represents the joint positions of the robot's fingers. $\sigma = 0.1$ is a scaling factor for distance normalization.

- **Reaching Object**

$$R_{\text{reaching_object}} = \left(1 - \tanh\left(\frac{\|\mathbf{p}_{\text{object}} - \mathbf{p}_{\text{ee}}\|_2}{\sigma}\right)\right) + \left(1 - \tanh\left(\frac{\|\mathbf{p}_{\text{object}} - \mathbf{p}_{\text{ee}}\|_2}{\sigma/4}\right)\right)$$

where $\mathbf{p}_{\text{object}}$ represents the position of the object in world coordinates. \mathbf{p}_{ee} represents the position of the end-effector in world coordinates. $\sigma = 0.2$ is a scaling factor for distance normalization.

- **Object Goal Tracking**

$$R_{\text{goal_tracking}} = \mathbb{1}(\mathbf{p}_{\text{object},z} > z_{\text{init}} + h_{\text{min}}) \left(1 - \tanh\left(\frac{\|\mathbf{p}_{\text{goal}} - \mathbf{p}_{\text{object}}\|_2}{\sigma}\right)\right)$$

where \mathbf{p}_{goal} represents the target position of the object in world coordinates. $\mathbf{p}_{\text{object}}$ represents the position of the object in world coordinates. $\mathbf{p}_{\text{object},z}$ represents the z -coordinate (height) of the object in world coordinates. z_{init} is the initial height of the object. $h_{\text{min}} = 0.02$ is the minimal height above the initial height required to achieve the goal. $\sigma = 0.3$ is a scaling factor for distance normalization.

- **Object Goal Tracking (Fine-Grained)**

$$R_{\text{goal_tracking_fine}} = \mathbb{1}(\mathbf{p}_{\text{object},z} > z_{\text{init}} + h_{\text{min}}) \left(1 - \tanh\left(\frac{\|\mathbf{p}_{\text{goal}} - \mathbf{p}_{\text{object}}\|_2}{\sigma_{\text{fine}}}\right)\right)$$

where \mathbf{p}_{goal} represents the target position of the object in world coordinates. $\mathbf{p}_{\text{object}}$ represents the position of the object in world coordinates. z_{init} is the initial height of the object. $h_{\text{min}} = 0.02$ is the minimal height above the initial height required to achieve the goal. $\sigma_{\text{fine}} = 0.05$ provides finer scaling for precise tracking.

- **Action Rate Penalty**

$$R_{\text{action_rate}} = -\|\mathbf{a}_t - \mathbf{a}_{t-1}\|_2^2$$

where \mathbf{a}_t represents the action at the current time step. \mathbf{a}_{t-1} represents the action at the previous time step.

- **Joint Velocity Penalty**

$$R_{\text{joint_vel}} = -\sum_{i \in \text{joint_ids}} \dot{q}_i^2$$

where \dot{q}_i represents the joint velocity of the i -th joint. joint_ids is the set of joint indices to penalize.

- **Contact Forces**

$$R_{\text{contact_forces}} = \mathbb{1}\left(\frac{\text{finger_dist}}{4} < \text{proj_len} < \frac{\text{finger_dist}}{1.25} + 0.2\right) \left(1.2 - \tanh\left(\frac{\text{object_dist}}{0.2}\right)\right) \mathbb{1}(\|\mathbf{p}_{\text{object}} - \mathbf{p}_{\text{top}}\| < 0.1) \left(1 - \tanh\left(\frac{\|\mathbf{org_vec} - \mathbf{y}\|}{0.3}\right)\right)$$

where $\mathbf{p}_{\text{top}}, \mathbf{p}_{\text{bottom}}, \mathbf{p}_{\text{left}}, \mathbf{p}_{\text{right}}$ are the positions of the robot's end-effector fingers (top, bottom, left, right) in world coordinates. $\mathbf{p}_{\text{object}}$ is the position of the object in world coordinates. $\mathbf{org_vec} = \mathbf{p}_{\text{left}} - \mathbf{p}_{\text{right}}$ is the vector between the left and right fingers, rotated into the object's local frame. $\mathbf{y} = [0, 1, 0]$ is the unit vector along the y-axis in the object's local frame. $\text{finger_dist} = \|\mathbf{p}_{\text{left}} - \mathbf{p}_{\text{right}}\|_2$ is the distance between the left and right fingers. $\text{proj_len} = \frac{(\mathbf{p}_{\text{object}} - \mathbf{p}_{\text{left}}) \cdot (\mathbf{p}_{\text{right}} - \mathbf{p}_{\text{left}})}{\text{finger_dist}}$ is the projection of the object's position onto the vector between the left and right fingers. $\text{object_dist} = \frac{\|\mathbf{p}_{\text{object}} - \mathbf{p}_{\text{bottom}} \times (\mathbf{p}_{\text{top}} - \mathbf{p}_{\text{bottom}})\|}{0.11}$ is the perpendicular distance from the object to the line formed by the bottom and top fingers.

- **Close Fingers**

$$R_{\text{close_fingers}} = \mathbb{1}(\text{grasp_force} > 0.5) \left(1 - \tanh \left(\frac{\sum_{i=1}^2 \text{finger_pos}[i]}{0.1} \right) \right)$$

where grasp_force represents the force exerted by the fingers on the object. finger_pos represents the joint positions of the robot's fingers.

- **Lift End Effector (EE)**

$$R_{\text{lift_ee}} = \frac{\text{clamp}(\mathbf{p}_{\text{ee},z} - 0.6, 0.0, 0.3)}{0.3} \cdot \mathbb{1}(\text{grasp_force} > 0.5)$$

where $\mathbf{p}_{\text{ee},z}$ represents the height of the end-effector above the ground.

- **Lift Object**

$$R_{\text{lift_object}} = \frac{\mathbb{1}(\mathbf{p}_{\text{object},z} > z_{\text{init}} + h_{\text{min}})}{\text{clamp}(\mathbf{p}_{\text{object},z} - z_{\text{init}} - h_{\text{min}}, 0.0, 0.2)} \cdot \frac{0.2}{0.2}$$

where $\mathbf{p}_{\text{object},z}$ represents the height of the object above the ground. z_{init} is the initial height of the object. $h_{\text{min}} = 0.02$ is the minimal height above the initial height required to achieve the goal.

Details of our weight design for the reward function can be found in Table 9:

Table 9: Reward Function Design

Reward Term	Weight
Fingers Open	5.0
Reaching Object	15.0
Object Goal Tracking	80.0
Object Goal Tracking (Fine-Grained)	70.0
Action Rate Penalty	-1e-4
Joint Velocity Penalty	-1e-4
Contact Forces	10
Close Fingers	100
Lift End Effector (EE)	20
Lift Object	100

F.2 Data Generation Details

In data generation, as shown in Fig. 2, we feed the images from the n_{cam} first-person cameras of the robot to YOLO-World at each timestep to detect the n_{obj} target objects to be manipulated, thus obtaining $n_{\text{cam}} * n_{\text{obj}}$ bounding boxes. Then we normalize the bounding box, concatenate them, and obtain a vector \mathbf{o} of dimension $4 * n_{\text{cam}} * n_{\text{obj}}$ as the visual feature input for the control policy. We then store the visual features $\mathbf{o}_t^{\text{vis}}$, all joint positions of the robot $\mathbf{o}_t^{\text{rob}}$, and actions \mathbf{a}_t for each step in the form of trajectories.

To reduce visual interference between parallel environments and minimize the sim-to-real gap, we incorporate a white room during data collection. The room is designed to be spacious enough

to accommodate the maximum working space, including robot, table, and apple. Three RGB-D cameras⁴, calibrated with intrinsic and extrinsic parameters matching those of the real robot, capture visual information. During inference, the images from these cameras are processed by YOLO-World to generate object bounding boxes.

Table 10: Camera Parameters

Camera	Link	Image Shape and Type
cam_high	fr_link6	Shape: [480, 640, 4] RGB, Range: 0-255 (torch.uint8)
cam_left_wrist	fl_link6	Shape: [480, 640, 4] RGB, Range: 0-255 (torch.uint8)
cam_right_wrist	fr_link6	Shape: [480, 640, 4] RGB, Range: 0-255 (torch.uint8)

Given the high memory demands of image data, we run 16 parallel environments on a single GPU⁵ for data generation, achieving up to 36k successful trajectories per day. For ACT training, these trajectories are subsequently stored in an HDF5 data structure⁶ (see Table 11). In our approach, we convert images to bounding boxes using YOLO-World and store the results in a dictionary format. Each trajectory consists of multiple steps, with each step containing bbox, qpos, and action data.

Table 11: HDF5 Data Structure

Group/Attribute	Dataset/Attribute Name	Description
Root Attributes	sim	Boolean indicating simulation (False)
	compress	Compression flag from ‘CollectEpsBuf’
Datasets	action	Array of actions taken
	reward	Array of rewards received
	base_action	Array of base actions
	base_action_t265	(Optional) Base actions from T265 sensor
Observations: states	qpos	Array of joint positions
	qvel	Array of joint velocities
	effort	Array of joint efforts
Observations: images	cam_high	Byte-encoded images from ‘cam_high’
	cam_left_wrist	Byte-encoded images from ‘cam_left_wrist’
	cam_right_wrist	Byte-encoded images from ‘cam_right_wrist’

E.3 Student Policy Details

We use RNN and ACT to train our student policy. The details of training parameters can be found in Table 12 and Table 13.

F.4 Sim2Real Technique

We employ the student policy for sim-to-real transfer, where the inputs to the policy included proprioception o_t^{rob} which consists of joint positions, and the visual input o_t^{vis} , represented by bounding boxes. The output action is the desired joint position for the next step. Thus, the primary sim-to-real gaps exist in the joint position and bounding box dimensions.

For joint positions, we develop a real-to-sim code that maps the joint positions obtained from teleoperation on a real-world robot to a simulated robot. We evaluate whether the actions performed at specific target positions were consistent between the real-world and simulated environments. For example, when teleoperating to grasp an apple at a precisely measured location, both the real-world

⁴But we only use RGB information.

⁵RTX4090D, 24GB.

⁶Video-based dataset

Table 12: RNN Training Parameters

Parameter	Value
lr	0.002
lr_backbone	7e-05
epochs	50
warmup_ratio	0.1
use_scheduler	cos
weight_decay	0.0001
loss_function	l1
hidden_dim	512
rnn_layers	3
rnn_hidden_dim	512
actor_hidden_dim	512
policy_class	RNN
gradient_accumulation_steps	1
random_mask_ratio	0.3

Table 13: ACT Training Parameters

Parameter	Value
num_epochs	1000
lr	4e-05
lr_backbone	7e-05
weight_decay	0.0001
kl_weight	10
backbone	resnet18
position_embedding	sine
loss_function	l1
chunk_size	32
hidden_dim	512
dim_feedforward	3200
enc_layers	4
dec_layers	7
nheads	8
dropout	0.2
train_loader_len	23
warmup_ratio	0.1
scheduler	cosine

and simulated apples are set at the same coordinates. We used the main arm of the real-world robot to observe whether the simulated robot could successfully grasp the apple.

Special handling is required for the gripper, as there are discrepancies between the URDF model of the gripper and its real-world counterpart. In the simulation, the gripper has two joints, while in reality, it functions as a single joint, leading to differences in value interpretation. To address this, we collect 10 data sets for fitting and utilize function interpolation to map the simulated gripper joint positions to those of the real-world gripper. This approach ensures that the state space and action space are aligned between the simulation and the real environment.

The sim-to-real gap for the bounding boxes corresponds to the image sim-to-real gap. We perform hand-eye calibration on the camera to ensure that the cameras in both the simulation and the real-world robot are approximately aligned. For finer adjustments, we select a specific point in front of the robot and a specific-sized object, observing the bounding boxes obtained from both the simulator and the real-world camera. Since we use bounding boxes, other factors, such as lighting and background variations in the Sim2Real gap are not a concern. Ultimately, this method of adjustment ensures that the intrinsic and extrinsic parameters of the camera are consistent between the simulation and the real-world environment.

G Hardware Details

The Mobile ALOHA robot is equipped with a dual-arm design, providing a total of 14 degrees of freedom (DoF), with 7 DoF per arm for versatile movement. It owns four arms in total: two for teleoperation during data collection and two subordinate arms that perform manipulation tasks. Each arm has a maximum valid payload of 1500g, and the gripper has a range of up to 80mm, allowing the robot to perform a variety of grasping and manipulation tasks efficiently. The detailed hardware information and an image of the robot can be found in Figure 27 and Table 14.

Table 14: Technical specifications.

Parameter	Value
Size	1080 × 700 × 1140
Arm weight	4.2 kg
Arm Payload	3000 g (peak) 1500 g (valid)
Arm reach	600 mm
Arm repeatability	1 mm
Arm working radius	653 mm
Joint motion range	J1: $\pm 154^\circ$, J2: $0^\circ \sim 165^\circ$ J3: $-175^\circ \sim 0^\circ$, J4: $\pm 106^\circ$ J5: $\pm 75^\circ$, J6: $\pm 100^\circ$
Gripper range	0-80 mm
Gripper max force	10 NM
DoF	$7 \times 2 = 14$

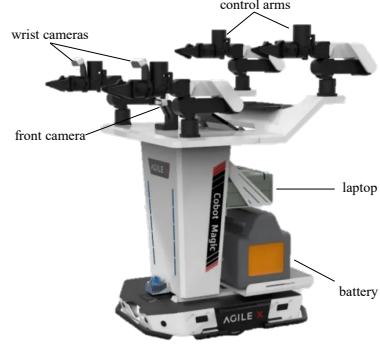


Figure 27: Hardware features.

H Limitations and Future Works

One of the limitations of ManiBox is that the accuracy of the obtained bounding box depends on the capability of the preceding visual model. As the YOLO-World sometimes may not be able to accurately partition the bounding box, ManiBox may grasp the wrong positions due to the wrong input bounding box. Also, the bounding box is mainly for objects with convex shapes and may be insufficient for handling flexible objects and fluids. In the future, a promising direction is to apply more powerful visual models like Grounding DINO and capture more semantic visual signals like segmentation via SAM in ManiBox to improve its ability. Also, for some complicated manipulation tasks like folding up clothes, directly training an RL teacher agent in the simulator may be difficult. Thus, how to utilize human demonstration or state machines to get the expert teacher agent is also worth researching.

I Broader Impacts

This work is about the basic theoretical algorithms of machine learning and robot control, so there is no particular broader impact to discuss.

J Experiments Compute Resources

All experiments are conducted on a single NVIDIA RTX 4090D GPU (24GB) and an Intel Core i7 (9th Generation) CPU. The training of the teacher policy requires approximately 45 minutes, while the data collection process for generating 36,000 trajectories takes around 24 hours. The student policy can be trained in under 10 minutes. For policy evaluation, generating 48 trajectories across 16 parallel environments takes approximately 30 minutes.

NeurIPS Paper Checklist

1. Claims

Question: Do the main claims made in the abstract and introduction accurately reflect the paper's contributions and scope?

Answer: [\[Yes\]](#)

Justification: The main claims of the paper are clearly stated in the abstract and further elaborated at the end of the introduction. The contributions are explicitly listed and align with the theoretical and experimental results presented in the paper. The scope of the work is well defined, including its assumptions and limitations.

Guidelines:

- The answer NA means that the abstract and introduction do not include the claims made in the paper.
- The abstract and/or introduction should clearly state the claims made, including the contributions made in the paper and important assumptions and limitations. A No or NA answer to this question will not be perceived well by the reviewers.
- The claims made should match theoretical and experimental results, and reflect how much the results can be expected to generalize to other settings.
- It is fine to include aspirational goals as motivation as long as it is clear that these goals are not attained by the paper.

2. Limitations

Question: Does the paper discuss the limitations of the work performed by the authors?

Answer: [\[Yes\]](#)

Justification: The limitations of the work can be found in Appendix H.

Guidelines:

- The answer NA means that the paper has no limitation while the answer No means that the paper has limitations, but those are not discussed in the paper.
- The authors are encouraged to create a separate "Limitations" section in their paper.
- The paper should point out any strong assumptions and how robust the results are to violations of these assumptions (e.g., independence assumptions, noiseless settings, model well-specification, asymptotic approximations only holding locally). The authors should reflect on how these assumptions might be violated in practice and what the implications would be.
- The authors should reflect on the scope of the claims made, e.g., if the approach was only tested on a few datasets or with a few runs. In general, empirical results often depend on implicit assumptions, which should be articulated.
- The authors should reflect on the factors that influence the performance of the approach. For example, a facial recognition algorithm may perform poorly when image resolution is low or images are taken in low lighting. Or a speech-to-text system might not be used reliably to provide closed captions for online lectures because it fails to handle technical jargon.
- The authors should discuss the computational efficiency of the proposed algorithms and how they scale with dataset size.
- If applicable, the authors should discuss possible limitations of their approach to address problems of privacy and fairness.
- While the authors might fear that complete honesty about limitations might be used by reviewers as grounds for rejection, a worse outcome might be that reviewers discover limitations that aren't acknowledged in the paper. The authors should use their best judgment and recognize that individual actions in favor of transparency play an important role in developing norms that preserve the integrity of the community. Reviewers will be specifically instructed to not penalize honesty concerning limitations.

3. Theory assumptions and proofs

Question: For each theoretical result, does the paper provide the full set of assumptions and a complete (and correct) proof?

Answer: [Yes]

Justification: The Lemma 3.1 and Lemma 3.2 have been fully stated in the main text 3.3 Simulation Data Generation. The detailed proofs are provided in Appendix A.1 and A.2.

Guidelines:

- The answer NA means that the paper does not include theoretical results.
- All the theorems, formulas, and proofs in the paper should be numbered and cross-referenced.
- All assumptions should be clearly stated or referenced in the statement of any theorems.
- The proofs can either appear in the main paper or the supplemental material, but if they appear in the supplemental material, the authors are encouraged to provide a short proof sketch to provide intuition.
- Inversely, any informal proof provided in the core of the paper should be complemented by formal proofs provided in appendix or supplemental material.
- Theorems and Lemmas that the proof relies upon should be properly referenced.

4. Experimental result reproducibility

Question: Does the paper fully disclose all the information needed to reproduce the main experimental results of the paper to the extent that it affects the main claims and/or conclusions of the paper (regardless of whether the code and data are provided or not)?

Answer: [Yes]

Justification: The source code is included in the supplementary materials, accompanied by detailed instructions for setting up the environment and reproducing all key experiments. This ensures that the main results and claims of the paper can be independently verified.

Guidelines:

- The answer NA means that the paper does not include experiments.
- If the paper includes experiments, a No answer to this question will not be perceived well by the reviewers: Making the paper reproducible is important, regardless of whether the code and data are provided or not.
- If the contribution is a dataset and/or model, the authors should describe the steps taken to make their results reproducible or verifiable.
- Depending on the contribution, reproducibility can be accomplished in various ways. For example, if the contribution is a novel architecture, describing the architecture fully might suffice, or if the contribution is a specific model and empirical evaluation, it may be necessary to either make it possible for others to replicate the model with the same dataset, or provide access to the model. In general, releasing code and data is often one good way to accomplish this, but reproducibility can also be provided via detailed instructions for how to replicate the results, access to a hosted model (e.g., in the case of a large language model), releasing of a model checkpoint, or other means that are appropriate to the research performed.
- While NeurIPS does not require releasing code, the conference does require all submissions to provide some reasonable avenue for reproducibility, which may depend on the nature of the contribution. For example
 - (a) If the contribution is primarily a new algorithm, the paper should make it clear how to reproduce that algorithm.
 - (b) If the contribution is primarily a new model architecture, the paper should describe the architecture clearly and fully.
 - (c) If the contribution is a new model (e.g., a large language model), then there should either be a way to access this model for reproducing the results or a way to reproduce the model (e.g., with an open-source dataset or instructions for how to construct the dataset).
 - (d) We recognize that reproducibility may be tricky in some cases, in which case authors are welcome to describe the particular way they provide for reproducibility. In the case of closed-source models, it may be that access to the model is limited in some way (e.g., to registered users), but it should be possible for other researchers to have some path to reproducing or verifying the results.

5. Open access to data and code

Question: Does the paper provide open access to the data and code, with sufficient instructions to faithfully reproduce the main experimental results, as described in supplemental material?

Answer: [Yes]

Justification: Refer to source code provided in supplemental material.

Guidelines:

- The answer NA means that paper does not include experiments requiring code.
- Please see the NeurIPS code and data submission guidelines (<https://nips.cc/public/guides/CodeSubmissionPolicy>) for more details.
- While we encourage the release of code and data, we understand that this might not be possible, so “No” is an acceptable answer. Papers cannot be rejected simply for not including code, unless this is central to the contribution (e.g., for a new open-source benchmark).
- The instructions should contain the exact command and environment needed to run to reproduce the results. See the NeurIPS code and data submission guidelines (<https://nips.cc/public/guides/CodeSubmissionPolicy>) for more details.
- The authors should provide instructions on data access and preparation, including how to access the raw data, preprocessed data, intermediate data, and generated data, etc.
- The authors should provide scripts to reproduce all experimental results for the new proposed method and baselines. If only a subset of experiments are reproducible, they should state which ones are omitted from the script and why.
- At submission time, to preserve anonymity, the authors should release anonymized versions (if applicable).
- Providing as much information as possible in supplemental material (appended to the paper) is recommended, but including URLs to data and code is permitted.

6. Experimental setting/details

Question: Does the paper specify all the training and test details (e.g., data splits, hyper-parameters, how they were chosen, type of optimizer, etc.) necessary to understand the results?

Answer: [Yes]

Justification: Full details are provided in the code.

Guidelines:

- The answer NA means that the paper does not include experiments.
- The experimental setting should be presented in the core of the paper to a level of detail that is necessary to appreciate the results and make sense of them.
- The full details can be provided either with the code, in appendix, or as supplemental material.

7. Experiment statistical significance

Question: Does the paper report error bars suitably and correctly defined or other appropriate information about the statistical significance of the experiments?

Answer: [Yes]

Justification: We report results averaged over three random seeds and include confidence bars representing the standard error of the mean.

Guidelines:

- The answer NA means that the paper does not include experiments.
- The authors should answer “Yes” if the results are accompanied by error bars, confidence intervals, or statistical significance tests, at least for the experiments that support the main claims of the paper.
- The factors of variability that the error bars are capturing should be clearly stated (for example, train/test split, initialization, random drawing of some parameter, or overall run with given experimental conditions).

- The method for calculating the error bars should be explained (closed form formula, call to a library function, bootstrap, etc.)
- The assumptions made should be given (e.g., Normally distributed errors).
- It should be clear whether the error bar is the standard deviation or the standard error of the mean.
- It is OK to report 1-sigma error bars, but one should state it. The authors should preferably report a 2-sigma error bar than state that they have a 96% CI, if the hypothesis of Normality of errors is not verified.
- For asymmetric distributions, the authors should be careful not to show in tables or figures symmetric error bars that would yield results that are out of range (e.g. negative error rates).
- If error bars are reported in tables or plots, The authors should explain in the text how they were calculated and reference the corresponding figures or tables in the text.

8. Experiments compute resources

Question: For each experiment, does the paper provide sufficient information on the computer resources (type of compute workers, memory, time of execution) needed to reproduce the experiments?

Answer: [\[Yes\]](#)

Justification: Details are provided in Appendix [J](#)

Guidelines:

- The answer NA means that the paper does not include experiments.
- The paper should indicate the type of compute workers CPU or GPU, internal cluster, or cloud provider, including relevant memory and storage.
- The paper should provide the amount of compute required for each of the individual experimental runs as well as estimate the total compute.
- The paper should disclose whether the full research project required more compute than the experiments reported in the paper (e.g., preliminary or failed experiments that didn't make it into the paper).

9. Code of ethics

Question: Does the research conducted in the paper conform, in every respect, with the NeurIPS Code of Ethics <https://neurips.cc/public/EthicsGuidelines>?

Answer: [\[Yes\]](#)

Justification: We have reviewed the NeurIPS Code of Ethics and confirm that our work adheres to all the guidelines. Our research does not involve any known ethical risks, and we have taken care to ensure responsible use of data, models, and reproducibility.

Guidelines:

- The answer NA means that the authors have not reviewed the NeurIPS Code of Ethics.
- If the authors answer No, they should explain the special circumstances that require a deviation from the Code of Ethics.
- The authors should make sure to preserve anonymity (e.g., if there is a special consideration due to laws or regulations in their jurisdiction).

10. Broader impacts

Question: Does the paper discuss both potential positive societal impacts and negative societal impacts of the work performed?

Answer: [\[Yes\]](#)

Justification: Discussed in Appendix [I](#)

Guidelines:

- The answer NA means that there is no societal impact of the work performed.
- If the authors answer NA or No, they should explain why their work has no societal impact or why the paper does not address societal impact.

- Examples of negative societal impacts include potential malicious or unintended uses (e.g., disinformation, generating fake profiles, surveillance), fairness considerations (e.g., deployment of technologies that could make decisions that unfairly impact specific groups), privacy considerations, and security considerations.
- The conference expects that many papers will be foundational research and not tied to particular applications, let alone deployments. However, if there is a direct path to any negative applications, the authors should point it out. For example, it is legitimate to point out that an improvement in the quality of generative models could be used to generate deepfakes for disinformation. On the other hand, it is not needed to point out that a generic algorithm for optimizing neural networks could enable people to train models that generate Deepfakes faster.
- The authors should consider possible harms that could arise when the technology is being used as intended and functioning correctly, harms that could arise when the technology is being used as intended but gives incorrect results, and harms following from (intentional or unintentional) misuse of the technology.
- If there are negative societal impacts, the authors could also discuss possible mitigation strategies (e.g., gated release of models, providing defenses in addition to attacks, mechanisms for monitoring misuse, mechanisms to monitor how a system learns from feedback over time, improving the efficiency and accessibility of ML).

11. Safeguards

Question: Does the paper describe safeguards that have been put in place for responsible release of data or models that have a high risk for misuse (e.g., pretrained language models, image generators, or scraped datasets)?

Answer: [NA]

Justification: The models and datasets used in this paper do not pose foreseeable risks of misuse or dual-use.

Guidelines:

- The answer NA means that the paper poses no such risks.
- Released models that have a high risk for misuse or dual-use should be released with necessary safeguards to allow for controlled use of the model, for example by requiring that users adhere to usage guidelines or restrictions to access the model or implementing safety filters.
- Datasets that have been scraped from the Internet could pose safety risks. The authors should describe how they avoided releasing unsafe images.
- We recognize that providing effective safeguards is challenging, and many papers do not require this, but we encourage authors to take this into account and make a best faith effort.

12. Licenses for existing assets

Question: Are the creators or original owners of assets (e.g., code, data, models), used in the paper, properly credited and are the license and terms of use explicitly mentioned and properly respected?

Answer: [Yes]

Justification: We used the IsaacLab codebase (version v1.2.0, commit e00d625), which is released under the BSD-3-Clause license. The official repository is available at <https://github.com/isaac-sim/IsaacLab>. We have properly credited the authors in our paper, and our use complies with the license terms.

Guidelines:

- The answer NA means that the paper does not use existing assets.
- The authors should cite the original paper that produced the code package or dataset.
- The authors should state which version of the asset is used and, if possible, include a URL.
- The name of the license (e.g., CC-BY 4.0) should be included for each asset.
- For scraped data from a particular source (e.g., website), the copyright and terms of service of that source should be provided.

- If assets are released, the license, copyright information, and terms of use in the package should be provided. For popular datasets, paperswithcode.com/datasets has curated licenses for some datasets. Their licensing guide can help determine the license of a dataset.
- For existing datasets that are re-packaged, both the original license and the license of the derived asset (if it has changed) should be provided.
- If this information is not available online, the authors are encouraged to reach out to the asset's creators.

13. New assets

Question: Are new assets introduced in the paper well documented and is the documentation provided alongside the assets?

Answer: [\[Yes\]](#)

Justification: The new assets are included in the code provided in supplementary materials.

Guidelines:

- The answer NA means that the paper does not release new assets.
- Researchers should communicate the details of the dataset/code/model as part of their submissions via structured templates. This includes details about training, license, limitations, etc.
- The paper should discuss whether and how consent was obtained from people whose asset is used.
- At submission time, remember to anonymize your assets (if applicable). You can either create an anonymized URL or include an anonymized zip file.

14. Crowdsourcing and research with human subjects

Question: For crowdsourcing experiments and research with human subjects, does the paper include the full text of instructions given to participants and screenshots, if applicable, as well as details about compensation (if any)?

Answer: [\[NA\]](#)

Justification: The paper does not involve crowdsourcing nor research with human subjects.

Guidelines:

- The answer NA means that the paper does not involve crowdsourcing nor research with human subjects.
- Including this information in the supplemental material is fine, but if the main contribution of the paper involves human subjects, then as much detail as possible should be included in the main paper.
- According to the NeurIPS Code of Ethics, workers involved in data collection, curation, or other labor should be paid at least the minimum wage in the country of the data collector.

15. Institutional review board (IRB) approvals or equivalent for research with human subjects

Question: Does the paper describe potential risks incurred by study participants, whether such risks were disclosed to the subjects, and whether Institutional Review Board (IRB) approvals (or an equivalent approval/review based on the requirements of your country or institution) were obtained?

Answer: [\[NA\]](#)

Justification: This work does not involve human subjects or crowdsourced data.

Guidelines:

- The answer NA means that the paper does not involve crowdsourcing nor research with human subjects.
- Depending on the country in which research is conducted, IRB approval (or equivalent) may be required for any human subjects research. If you obtained IRB approval, you should clearly state this in the paper.

- We recognize that the procedures for this may vary significantly between institutions and locations, and we expect authors to adhere to the NeurIPS Code of Ethics and the guidelines for their institution.
- For initial submissions, do not include any information that would break anonymity (if applicable), such as the institution conducting the review.

16. Declaration of LLM usage

Question: Does the paper describe the usage of LLMs if it is an important, original, or non-standard component of the core methods in this research? Note that if the LLM is used only for writing, editing, or formatting purposes and does not impact the core methodology, scientific rigorousness, or originality of the research, declaration is not required.

Answer: [NA]

Justification: The core method development in this research does not involve LLMs as any important, original, or non-standard components.

Guidelines:

- The answer NA means that the core method development in this research does not involve LLMs as any important, original, or non-standard components.
- Please refer to our LLM policy (<https://neurips.cc/Conferences/2025/LLM>) for what should or should not be described.